

REMARKS

Examiner has objected to Applicant's new drawing Figure 1A as introducing new matter. Specifically, Examiner has stated that there is no support in the original disclosure, as filed, for the relative sizes and positional relationships of each component of the drawing.

In response to Examiner's objection, Applicant respectfully submits that **no** new matter has been introduced. To begin, under **37 CFR 1.84, Standards for Drawings, subsection (k), Scale**, "the scale to which a drawing is made must be large enough to show the mechanism without crowding when the drawing is reduced in size to two-thirds in reproduction. Indications such as "actual size" or "scale 1/2" on the drawings are not permitted since these lose their meaning with reproduction in a different format." As such, Applicant is neither required nor necessarily permitted to delineate or illustrate "relative sizes", as indicated by Examiner. Under **37 CFR 1.84**, Applicant is simply required to show in the drawings all features of the claims. Applicant's drawing Figure 1A could hardly be considered as introducing new matter, since the matter appeared in Applicant's originally filed specification and claims. Additionally, the positional relationship of the various components of Applicant's apparatus was not, and is not, intended to be a limiting factor of Applicant's invention. Indeed, the positional relationship amongst the various components of Applicant's apparatus is a function of engineering, design choice, and relative sizes of each component (this latter issue being addressed hereinabove). Reconsideration is respectfully requested.

Examiner has further objected to the drawing Figure 1A, stating that Applicant has improperly designated the ANODE and CATHODE. In response thereto, Applicant

directs Examiner's attention to the enclosed Replacement Sheet. Reconsideration is respectfully requested.

Applicant respectfully asserts that it was Examiner who, in his last Office Action, required submittal of a drawing sheet or corrected drawing sheet illustrating the originally claimed subject matter – yet now, Examiner objects to same. Applicant has only included in Figure 1A an illustration of the components requested by Examiner and appearing in the originally presented claims. Applicant cannot simply randomly place onto a sheet its various components with no association or relationship. Indeed, Figure 1A, and the amended specification associated therewith, is simply intended to illustrate the functional, and not necessarily the structural, relationship between Applicant's various components – such a functional relationship was made clear and originally presented in the claims and specification.

In a related matter, Examiner has objected to Applicant's amendment to the specification filed on 09/27/2005, asserting that the amendment introduces new matter. Applicant presumes that Examiner's contention is similarly based on his grounds for objecting to the drawing Figure 1A. However, Applicant again respectfully notes that all components of Applicant's invention, and the functional relationships therebetween, were described and fully disclosed throughout Applicant's originally filed specification and claims. Applicant's 09/27/2005 specification amendment only assigns reference characters to previously disclosed subject matter – all for purposes of understanding the functional, and not necessarily the structural, relationship, amongst the originally claimed components now presented in Figure 1A. As such, no new matter has been added.

Indeed, Applicant's amendments to the specification and drawings are clearly within contemplation of the Patent rules and laws. To provide Examiner with support of such amendments, Applicant respectfully directs Examiner's attention to the arguments of section A-C presented hereinbelow. However, Applicant initially directs Examiner's attention to **MPEP 2163.06, Relationship of Written Description Requirement to New Matter**, which states that information contained in any one of the specification, claims or drawings of the application as filed **may be added to any other part of the application without introducing new matter**. Furthermore, the claims as filed in the original specification are part of the disclosure and, therefore, if an application as originally filed contains a claim disclosing material not found in the remainder of the specification, the applicant may amend the specification to include the claimed subject matter. *In re Benno*, 768 F.2d 1340, 226 USPQ 683 (Fed. Cir. 1985).

Accordingly, in the present case, Applicant's amendments to the specification and drawings do not introduce new matter, as the information was originally contained in the claims, as filed. Examiner's rejections based on new matter are wholly improper. Reconsideration is respectfully requested.

Examiner has further broadly objected to the specification as failing to provide adequate written description and as failing to provide an enabling disclosure. Examiner has still further broadly rejected the claims as failing to point out and distinctly claim the subject matter which Applicant regards as his invention. Applicant addresses Examiner's broad objections and rejections in following arguments.

To begin generally, however, Examiner has asserted that the specification fails to disclose the meets and bounds of the limitation "atomically sharp" and that such does not

connote the same meaning as having only one atom at the apex. Examiner utilizes the foregoing argument as a platform for launching many of his rejections throughout the Office Action, in addition to various assertions that an apex comprising one atom cannot be manufactured and/or that Applicant has not shown that such is possible of manufacture and/or even known within the art. Moreover, on Page 7 of the present Office Action, Examiner states that because Applicant has proposed a new method of manufacture, such indicates that Applicant has not actually reduced to practice or “proved” his invention – **such is not required under the law**. Examiner continues with various other rejections based on an assertion that Applicant fails to adequately disclose or teach an operative device or technology.

In response to Examiner’s rejections, Applicant directs Examiner’s attention to the arguments presented hereinbelow, which Applicant respectfully asserts clarify Applicant’s requirements under the Patent statutes and, thus, the concordant impropriety of Examiner’s rejections and objections that apparently run contradictory to said statutes, and contradictory to well-established law. Applicant’s original disclosure, original filing, current evidence, and current arguments clearly demonstrate that Applicant has satisfied his statutory requirements.

In addition to the following arguments, all presented in support of originally claimed and amended subject matter (i.e., atomically sharp), and presented in response to Examiner’s rejections/objections, Applicant respectfully directs Examiner’s attention to the attached articles and documents that clearly and undisputedly show that the term “atomically sharp” is well-understood and well-accepted within the art.

Applicant respectfully requests that Examiner consider the foregoing and the following arguments in view of the fact that Examiner has **not**, to date, shown, through evidence or otherwise, that one of ordinary skill in the art would reasonably doubt the asserted utility **of Applicant's specific invention** - not the concept of cold fusion - (which has already been denounced by Applicant) - but rather Applicant's specifically claimed apparatus and method of heat fusion. That is, Examiner has failed to provide any reference that specifically discloses Applicant's components and/or that specifically discloses the alleged inoperability of Applicant's invention. Instead, Examiner has improperly shifted his burden of proof onto Applicant by simply characterizing and asserting that Applicant's invention is one of cold fusion, and, in support of his assertion, Examiner only provides references directed toward cold fusion - none of which even disclose or fairly suggest the structural or functional features, components, and associated relationships, in Applicant's invention. Such examination procedures are improper and contrary to well-established procedure.

A. Written Description & Enablement Requirements:

Applicant respectfully directs Examiner's attention to **MPEP 2164 The Enablement Requirement [R-2]**: The purpose of the enablement requirement is that the specification describe the invention in such terms that one skilled in the art can make and use the claimed invention is to ensure that the invention is communicated to the interested public in a meaningful way. The information contained in the disclosure of an application must be **sufficient to inform those skilled in the relevant art** how to both make and use the claimed invention. However, to comply with 35 U.S.C. 112, first

paragraph, it is not necessary to "enable one of ordinary skill in the art to make and use a perfected, commercially viable embodiment absent a claim limitation to that effect." *CFMT, Inc. v. Yieldup Int'l Corp.*, 349 F.3d 1333, 1338, 68 USPQ2d 1940, 1944 (Fed. Cir. 2003) (an invention directed to a general system to improve the cleaning process for semiconductor wafers was enabled by a disclosure showing improvements in the overall system). Detailed procedures for making and using the invention may not be necessary if the description of the invention itself is sufficient to permit those skilled in the art to make and use the invention."

The enablement requirement of 35 U.S.C. 112, first paragraph, is separate and distinct from the description requirement. *Vas-Cath, Inc. v. Mahurkar*, 935 F.2d 1555, 1563, 19 USPQ2d 1111, 1116-17 (Fed. Cir. 1991) ("the purpose of the 'written description' requirement is broader than to merely explain how to 'make and use'"). See also MPEP § 2161. Therefore, the fact that an additional limitation to a claim may lack descriptive support in the disclosure as originally filed does not necessarily mean that the limitation is also not enabled. In other words, the statement of a new limitation in and of itself may enable one skilled in the art to make and use the claim containing that limitation even though that limitation may not be described in the original disclosure.

Not everything necessary to practice the invention need be disclosed. In fact, what is well-known is best omitted. *In re Buchner*, 929 F.2d 660, 661, 18 USPQ2d 1331, 1332 (Fed. Cir. 1991). All that is necessary is that one skilled in the art be able to practice the claimed invention, given the level of knowledge and skill in the art. Further

the scope of enablement must only bear a "reasonable correlation" to the scope of the claims. See, e.g., *In re Fisher*, 427 F.2d 833, 839, 166 USPQ 18, 24 (CCPA 1970).

Additionally, with reference to **MPEP 2164.03, Relationship of Predictability of the Art and the Enablement Requirement [R-2]**, the amount of guidance or direction needed to enable the invention is inversely related to the amount of knowledge in the state of the art as well as the predictability in the art. *In re Fisher*, 427 F.2d 833, 839, 166 USPQ 18, 24 (CCPA 1970). The "amount of guidance or direction" refers to that information in the application, as originally filed, that teaches exactly how to make or use the invention. **The more that is known in the prior art about the nature of the invention, how to make, and how to use the invention, and the more predictable the art is, the less information needs to be explicitly stated in the specification.** As such, Applicant's teachings and disclosures of "atomically sharp" and nanotechnology are sufficiently enabled in view of the amount of knowledge in the state of the art, as demonstrated by the enclosed articles and documents, and Applicant's previously submitted documents.

Nonetheless, Applicant recognizes that under **MPEP 2164.05 Determination of Enablement Based on Evidence as a Whole**, once the examiner has weighed all the evidence and established a reasonable basis to question the enablement provided for the claimed invention, the burden falls on Applicant to present persuasive arguments, **supported by suitable proofs where necessary**, that one skilled in the art would be able to make and use the claimed invention using the application as a guide. *In re Brandstadter*, 484 F.2d 1395, 1406-07, 179 USPQ 286, 294 (CCPA 1973). **The evidence provided by applicant need not be conclusive but merely convincing to one skilled in**

the art. Applicant respectfully submits that the attached articles and documents provide such suitable proof.

Again, the specification need not disclose what is well-known to those skilled in the art and **preferably omits that which is well-known** to those skilled and already available to the public. *In re Buchner*, 929 F.2d 660, 661, 18 USPQ2d 1331, 1332 (Fed. Cir. 1991); *Hybritech, Inc. v. Monoclonal Antibodies, Inc.*, 802 F.2d 1367, 1384, 231 USPQ 81, 94 (Fed. Cir. 1986), *cert. denied*, 480 U.S. 947 (1987); and *Lindemann Maschinenfabrik GMBH v. American Hoist & Derrick Co.*, 730 F.2d 1452, 1463, 221 USPQ 481, 489 (Fed. Cir. 1984).

The state of the art existing at the filing date of the application is used to determine whether a particular disclosure is enabling as of the filing date. *Chiron Corp. v. Genentech Inc.*, 363 F.3d 1247, 1254, 70 USPQ2d 1321, 1325-26 (Fed. Cir. 2004). Applicant respectfully submits that the attached articles and documents demonstrate that the state of the art existing at the filing date teaches that the term “atomically sharp” is well-known amongst those ordinarily skilled within the art.

B. Reduction to Practice; Working Examples; Proof:

Additionally, Applicant respectfully directs Examiner’s attention to **MPEP 2164.02 Working Example**: compliance with the enablement requirement of **35 U.S.C. 112**, first paragraph, does not turn on whether an example is disclosed. An example may be “working” or “prophetic.” A working example is based on work actually performed. **A prophetic example describes an embodiment of the invention based on predicted results rather than work actually conducted or results actually achieved.**

An applicant need not have actually reduced the invention to practice prior to filing. In *Gould v. Quigg*, 822 F.2d 1074, 1078, 3 USPQ 2d 1302, 1304 (Fed. Cir. 1987), as of Gould's filing date, no person had built a light amplifier or measured a population inversion in a gas discharge. The Court held that "**The mere fact that something has not previously been done clearly is not, in itself, a sufficient basis for rejecting all applications purporting to disclose how to do it.**" 822 F.2d at 1078, 3 USPQ2d at 1304 (quoting *In re Chilowsky*, 229 F.2d 457, 461, 108 USPQ 321, 325 (CCPA 1956)).

Under MPEP 2138.05 "Reduction to Practice" [R-3], reduction to practice may be an actual reduction or a constructive reduction to practice which occurs when a patent application on the claimed invention is filed. The filing of a patent application serves as conception and constructive reduction to practice of the subject matter described in the application. **Thus the inventor need not provide evidence of either conception or actual reduction to practice when relying on the content of the patent application.** *Hyatt v. Boone*, 146 F.3d 1348, 1352, 47 USPQ2d 1128, 1130 (Fed. Cir. 1998).

Examiner requires of Applicant to make showings contrary to well-established law. Such is unfair and abusive.

C. Operability of the Invention

The examiner has the initial burden of challenging an asserted utility. Only after the examiner has provided evidence showing that one of ordinary skill in the art would reasonably doubt the asserted utility does the burden shift to the applicant to provide rebuttal evidence sufficient to convince one of ordinary skill in the art of the invention's

asserted utility. *In re Swartz*, 232 F.3d 862, 863, 56 USPQ2d 1703, 1704 (Fed. Cir. 2000); *In re Brana*, 51 F.3d 1560, 1566, 34 USPQ2d 1436, 1441 (Fed. Cir. 1995) (citing *In re Bundy*, 642 F.2d 430, 433, 209 USPQ 48, 51 (CCPA 1981)).

In the present case, Examiner has not provided any references that undisputedly show that Applicant's specifically disclosed and claimed apparatus and method is inoperable. Examiner has not shown any reference that teaches Applicant's components and the functional relationships thereamongst, or that such an arrangement of Applicant's specific components would result in an inoperable invention. Applicant queries how it is possible for Examiner to even question the asserted utility and operability of Applicant's invention, when Examiner has failed to provide any evidence demonstrating otherwise. Examiner cannot, absent applicable references, opine alone as to the operability or utility of Applicant's invention. Such opinions must be based on references that prove Applicant's claimed apparatus, method and associated features, components and arrangements are inoperable, would tend not to function, or otherwise raise questions as to the utility of Applicant's claimed invention. The reference of systems that are functionally and structurally non-analogous to Applicant's invention does not meet this burden.

D. Technical/Scientific Arguments and Analysis:

As previously noted by Applicant, "atomically sharp" is a well-known term in the literature. In support of Applicant's assertion, attached is a 1998 paper on "Vacuum Tunneling of Superconducting Quasiparticles from Atomically Sharp Scanning Tunneling Microscope Tips" by Pan et al., presented only to show use of the term. The

term is essentially defined in the fourth sentence of the article. Nothing else in the article is meant to pertain to the present invention.

Examiner, in the previous office action, has referenced a number of existing patents, which profess to show sharp and pointed tips, with the allegation that the present invention is included in such. Unless one utilizes highly specialized techniques for nanoassembly, only available within the last 10 or so years, it is not possible to manufacture such an atomically sharp tip. Thus, previous “sharp tip” patents are, by their nature, manufactured in a way that is NOT atomically sharp, but rather blunt, defeating the necessary geometry for the tip charge density required. Even the best manufacturing technique for surfaces, typically used for optical flatness, only produces a surface flat to within $1/20$ wavelength of light (typically 700 nm), thus having a surface roughness of 35nm. For an atomic dimension of 0.2 nm, a 35nm surface roughness is mountainous and jagged, and not atomically flat. Clearly, for a less precise manufacturing technique for tip creation, one will not attain atomic sharpness; thus, the patents referenced by the Examiner are NOT inclusive of the present invention.

The Examiner has suggested that the prior reference of the effects of electron screening was inapplicable as it pertained to astrophysical phenomena. In response thereto, Applicant attaches a 2003 paper entitled “Enhancement of Nuclear Reactions Due to Screening Effects of Core Electrons” by Luo et al., which is particularly applicable to deuterium-deuterium reactions. It is noted that this paper includes references 6-8, noted research papers from 1998 through 2002, which address the effect of electron screening on nuclear reaction rate.

Examiner has further suggested that the fabrication of the cones is not within the invention specification. In addition to the arguments presented hereinabove, Applicant notes that Pedraza et al., "Surface Nanostructuring of Silicon" (2003) shows how irradiation with laser will produce nano-cones on a silicon surface, controllable by the parameters of the experiment. Additionally, Seeger and Palmer, "Fabrication of Silicon Cones and Pillars Using Rough Metal Films" (1998) uses reactive ion etching to produce trillions of nanoscale silicon cones, with pillar diameters as small as 5nm. Such reactive ion etching is also shown in Wellner et al., "Mechanisms of Visible Photoluminescence from Nanoscale Silicon Cones" (2002), which illustrates the use of silver films as etch masks. Periodic nanostructures, in this case ripples, have been produced by focused ion beam, as outlined by Xie et al., in "Fabrication and Thermal Annealing Behavior of Nanoscale Ripple Fabricated by Focused Ion Beam" (2003). Accordingly, Applicant reiterates that technology well known within the art does not require explicit treatment within the specification – such is a recognized principle of patent law.

To further illustrate the ease of fabrication of the cones, Lei et al., in "Fabrication, Characterization and Physical Properties of Nanostructured Metal Replicated Membranes" (2003) shows, in Figure 1, a method of electrical etching (i.e. anodization) and palladium deposition, and also illustrates the use in Fig 1(h)-(j) of electrolytic metallic deposition, as referenced in the present patent application. The technique of electroless metallization has been published, to Applicant's knowledge, since the year 2000. This assertion is supported by reference 22 within the article by Kudo and Fujihara "DNA-Templated Copper Nanowire Fabrication by a Two-Step Process Involving Electroless Metalization. It is noted that this article was published recently, postdating

the patent application, **but the technique of electroless metallization referenced predates the patent application.**

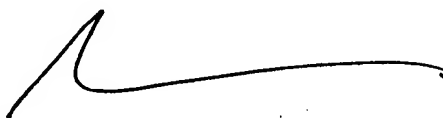
Finally, Applicant attaches a photograph of the actual material surface utilized in fabrication of the present invention. This particular surface is atomically flat mica with a gold overcoating packed in argon gas. Hydrogen annealing of the gold will produce an atomically flat surface, to be subsequently formed to cones by either the laser physical processes or the chemical etching processes outlined above.

Applicant respectfully submits that the foregoing arguments demonstrate the propriety of Applicant's specification and claims, and the satisfaction of the applicable Patent statutes. Applicant respectfully requests that Examiner withdraw his current objections/rejections of the drawings, specification and claims, and/or provide Applicant with references that support Examiner's arguments.

CONCLUSION

The above-made arguments and amendments are to form only and thus, no new matter was added. Applicant respectfully believes the above-made arguments and amendments now place the Claims and application in condition for allowance. Should there be any questions or concerns, the Examiner is invited to telephone Applicant's undersigned attorney.

Respectfully submitted this 4th day of April, 2006.



Ashish D. Patel, Esq.
Reg. No. 50,177

Myers & Kaplan,
Intellectual Property Law, L.L.C.
1899 Powers Ferry Road
Suite 310
Atlanta, GA 30339
Phone: 770-541-7444
Fax: 770-541-7448
E-mail: apatel@mkiplaw.com

DNA-Templated Copper Nanowire Fabrication by a Two-Step Process Involving Electroless Metallization

Hidetoshi Kudo and Masamichi Fujihira

Abstract—Here, we report a new fabrication method of DNA-templated copper nanowires. The copper nanowires were fabricated via two-step reactions. First, Pd(II) ions were electrostatically adsorbed onto negatively charged DNA molecules immobilized on the substrate surfaces and reduced chemically. As a result, palladium nanowires with a diameter of approximately 6 nm were obtained. Second, the palladium nanowires were dipped into a copper electroless plating bath. Electroless deposition of copper proceeded specifically on the palladium nanowires. The diameters of the copper nanowires were controlled by the plating time.

Index Terms—Copper, DNA, nanotechnology, palladium.

I. INTRODUCTION

NEW techniques of bottom-up lithography have been investigated because of the lower limit of nanosize fabrication by top-down lithography, e.g., photolithography. Bottom-up lithography is a fabrication of nanostructures by integrating atoms, molecules, and particles. DNA molecules have been explored as one of the candidates of building blocks for the bottom-up methods, especially as connecting wires in nanoelectronics [1], [2], because of their specific molecular recognition capability and large aspect ratio. However, their intrinsic conductance has been considered to be low [3]–[7]. To increase their conductance, metals, e.g., gold [8], [9], silver [3], [10], [11], copper [11], [12], platinum [13], [14], and palladium [15]–[18], have been deposited on DNA molecules. In [11] and [12], a fabrication method of copper nanowires was demonstrated by predeposition of Cu^{2+} ions followed by their reduction. However, this method without electroless plating was unsuitable for fabrication of the copper nanowires deposited continuously with a diameter of more than ~ 4 nm.

Here, we show a new, simple fabrication method of DNA-templated continuous copper nanowires. The method is based on two-step reactions involving activation with palladium and electroless plating of copper. The copper electroless plating proceeds specifically on palladium. The diameters of the copper nanowires can be easily controlled from the minimum of a few nanometers by plating time.

Manuscript received March 13, 2005; revised August 19, 2005. This work was supported by the Ministry of Education, Science, Sports, and Culture of Japan under a Grant-in-Aid for Creative Scientific Research on "Devices on molecular and DNA levels" 13GS0017.

The authors are with the Department of Biomolecular Engineering, Tokyo Institute of Technology, Yokohama 226-8501, Japan (e-mail: hkudou@bio.titech.ac.jp; mfuji@bio.titech.ac.jp).

Digital Object Identifier 10.1109/TNANO.2006.869691

II. EXPERIMENTS

A. Materials

Octadecyltrimethoxysilane (OTS) (Tokyo Kasei), lambda bacteriophage DNA (λ -DNA) (Takara Bio Inc.), TE buffer (Dojindo), formaldehyde 37 wt% (Sigma), palladium(II) acetate (Sigma-Aldrich), borane-dimethylamine complex (Aldrich), 85% lactic acid, trisodium citrate dihydrate, ammonia solution, copper(II) sulfate pentahydrate, potassium sodium (+)-tartrate tetrahydrate, and sodium hydroxide (Kanto Chemical) were used without further purification. Deionized water ($18.2 \text{ M}\Omega \cdot \text{cm}$) prepared with a Millipore system was used throughout the experiments.

B. Immobilization of DNA Molecules on Substrate

Glass cover slips (Matsunami Glass) silanized with OTS were used as substrates [19]. DNA molecules were stretched on the substrate surfaces by an immobilization process called the dynamic molecular combing method [19], [20]. We used double-stranded λ -DNA. The DNA molecules were diluted to $30 \text{ ng}/\mu\text{L}$ with a TE buffer (10 mM Tris-HCl, 1 mM EDTA, pH 8.0). The silanized substrate was vertically dipped into the solution at 3.4 mm/s using a mechanical apparatus. After incubation for 3 min, the silanized substrate was lifted up from the solution at a constant speed of $300 \mu\text{m/s}$. The DNA molecules were stretched by the water capillary force at an air-solution-substrate interface [20] and immobilized on the substrate surface by physical adsorption [21].

C. Activation With Palladium

The activation step, i.e., palladium deposition, was carried out according to the literature [16], [18]. A Pd^{2+} solution was prepared by dissolving 5.0 mg of palladium acetate in 1-mL deionized water by sonication for 5 min followed by centrifugation at 9000 r/min for 5 min to obtain a saturated solution and to separate undissolved particles. The substrate on which DNA molecules were stretched and immobilized was vertically dipped into the palladium acetate solution at 3.4 mm/s . After incubation for 10 s, it was lifted up from the solution at 3.4 mm/s . Afterwards, it was vertically dipped at 3.4 mm/s into a reduction bath containing 2.5 g/L of sodium citrate, 2.5 g/L of 85% lactic acid, and 0.25 g/L of borane-dimethylamine complex with pH 7.4 adjusted by ammonia solution. After incubation for 30 s, it was lifted up from the reduction bath at 3.4 mm/s .

D. Electroless Plating of Copper

A copper electroless plating bath contained 30 g/L of CuSO_4 , 140 g/L of sodium potassium tartrate, 20 g/L of NaOH, and 10 mL/L of formaldehyde [22]. The bath solution was immediately used because of its instability. The substrate with the DNA

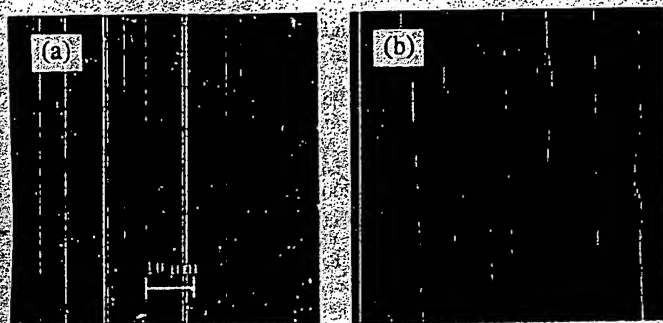


Fig. 1. (a) Fluorescence microscopic and (b) AFM topographic images of combed DNA molecules. Scan size and height scale of the AFM image are $10\ \mu\text{m} \times 10\ \mu\text{m}$ and 3.3 nm, respectively.

molecules activated by palladium was vertically dipped into the bath at 3.4 mm/s. After incubation for 0–25 s, it was lifted up from the bath at 3.4 mm/s. The maximum dipping and lifting speed of the mechanical apparatus of 3.4 mm/s was used for accurate control of the reaction times for the palladium activation and the electroless plating.

E. Observation by Atomic Force Microscopy

All samples (i.e., silanized substrates, stretched DNA molecules, DNA molecules activated by palladium, and those after electroless deposition of copper) were observed in the air at room temperature with an SPA400 atomic force microscope (AFM) unit and an SPI3800N control station (Seiko Instruments) operated in tapping mode. The AFM probes were 225- μm -long monocrystalline silicon cantilevers (NanoWorld) with a normal spring constant of 31–71 N/m and a resonance frequency of 170–210 kHz.

III. RESULTS AND DISCUSSION

The DNA molecules were stretched and immobilized by the dynamic molecular combing method [20] on the glass cover slips silanized with OTS. Fig. 1(a) is a fluorescence microscopic image of DNA molecules stained with YOYO-1. Average length of the stretched molecule is about 25.8 μm (1.88 kbp/ μm). Due to hydrophobicity of the silanized surface, removal of residual solution from the surface, e.g., blowing air or absorbing with filter paper, after lifting up from each solution is not required. Density of the combed DNA molecules (approximately 180 molecules/ $10^4\ \mu\text{m}^2$) was not changed appreciably by immersing the substrate with immobilized DNA in the Pd^{2+} solution, the reduction bath, and the copper electroless plating bath. Fig. 1(b) is an AFM topographic image of the combed DNA molecule. The heights of the DNA molecules measured by AFM were approximately 1.7 nm. We estimated diameters of DNA molecules or nanowires throughout this study by measuring not widths but heights, because observed heights were not affected by tip-sample convolution.

Fig. 2(a) and (b) shows AFM topographic images of a DNA molecule after immersion into the Pd^{2+} solution and the reduction bath and after further copper electroless deposition for 20 s, respectively. We can see that palladium and copper clusters grew along the DNA molecule. Fig. 2(a') and (b') are cross sections along lines in Fig. 2(a) and (b), respectively. From the cross sections, the heights of the DNA molecules after such treatments were (a) 5.4 and (b) 19.7 nm, respectively. After the copper electroless plating, the height was obviously increased.

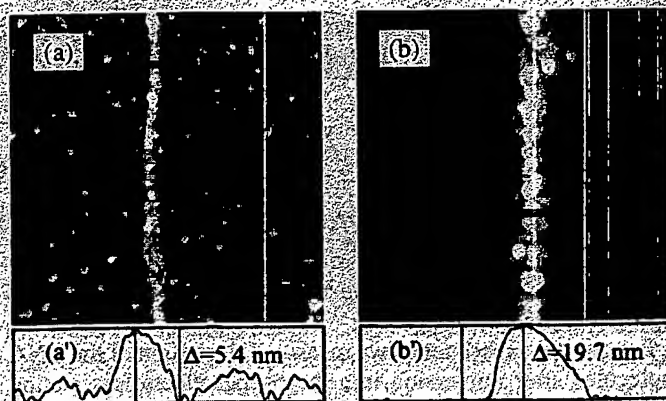


Fig. 2. 500 nm \times 500 nm AFM topographic images of a DNA molecule: (a) after palladium activation and (b) after palladium activation/copper electroless deposition. (a') and (b') are cross sections corresponding to the line drawn in the AFM images (a) and (b), respectively. Height scale: (a) 6.7 nm and (b) 22.6 nm.

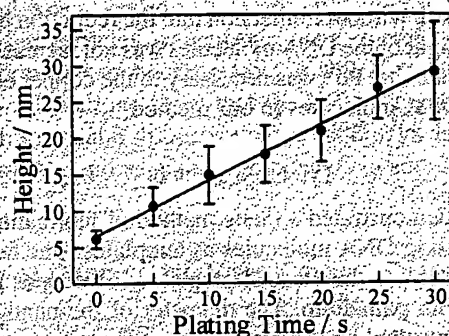


Fig. 3. Time dependence of the diameter of nanowires for the copper electroless plating.

Fig. 2(a) shows high nonspecific background. This can be attributed to $-\text{O}^-$ groups on the glass substrate surface. A part of $-\text{OH}$ groups on the glass substrate surface remain unreacted even after silanization and dissociate into $-\text{O}^-$ at higher pH than the isoelectric point of glass ($> \text{pH } 2$) [21]. Hence, palladium ions adsorb onto the silanized glass substrate in the palladium acetate solution (approximately pH 4.2). The nonspecific background reduces in Fig. 2(b). It is likely that the high internal stress of the electroless copper leads to delamination once the total stress of the electroless copper exceeds the adhesion strength [23].

Fig. 3 shows the average height as the diameter of the copper nanowires increases as a function of plating time. The error bar due to nonuniformity of nanowires as clearly shown in Fig. 2 is slightly increasing with the plating time. It is likely that this reflects variation in plating rate depending on nonuniformity of the nanowires. The average plating rate was found to be approximately 0.75 nm/s. This value is consistent with that reported previously (1–5 $\mu\text{m}/\text{h}$) [24]. These results indicate that copper nanowires were successfully fabricated. Chemical analysis of the nanowires will be performed in the near future.

Fig. 4 is a wide AFM image of copper nanowire consisting of four trimmings of $10\ \mu\text{m} \times 10\ \mu\text{m}$ AFM images. We can see that the copper was deposited continuously over the whole DNA molecule. The gaps between metals were not observed even in the magnified image shown in Fig. 2(b). Although the length of λ -DNA in the unstretched form can be 16.5 μm (0.34 nm/bp \times 48 502 bp) [25], the nanowires of 20 μm or more in the length were observed. This observation supports that the

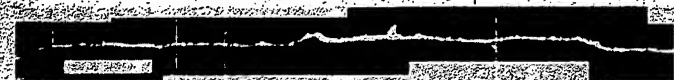


Fig. 4. AFM topographic image of the copper nanowire (plating time = 20 s). Height scale: 20 nm; scale bar: 2 μ m.

DNA molecules were stretched during the dynamic molecular combing [19]. As another possibility, DNA molecules might overlap each other because the DNA concentration used was high in the present study.

For control experiments, we measured the height of the DNA molecules after immersion into the copper electroless plating bath without palladium activation, i.e., without immersion into the Pd^{2+} solution and the reduction bath. We confirmed that the height of the DNA molecules was not increased even after immersion into the plating bath for 3 min. We also measured height of DNA molecules after immersion into the Pd^{2+} solution and the plating bath without immersion into the reduction bath. Similarly, the height of the DNA molecules was not increased. These results indicate that Pd^0 was necessary to the copper electroless plating on DNA molecules in our method.

IV. CONCLUSION

We have demonstrated a facile method of fabricating copper nanowires using DNA molecules as templates. The fabrication takes advantage of the electroless plating of copper including activation with palladium. The diameter of the nanowires can be easily controlled by the plating time. The nanowires are attractive materials for future nanoelectronic devices.

REFERENCES

- [1] J. Richter, "Metallization of DNA," *Physica E*, vol. 16, pp. 157–173, 2003.
- [2] R. M. Stoltenberg and A. T. Woolley, "DNA-templated nanowire fabrication," *Biomed. Microdevices*, vol. 6, pp. 105–111, 2004.
- [3] E. Braun, Y. Eichen, U. Sivan, and G. Ben-Yoseph, "DNA-templated assembly and electrode attachment of a conducting silver wire," *Nature*, vol. 391, pp. 775–778, 1998.
- [4] P. J. de Pablo, F. Moreno-Herrero, J. Colchero, J. Gómez Herrero, P. Herrero, A. M. Baró, P. Ordejón, J. M. Soler, and E. Artacho, "Absence of DC-conductivity in λ -DNA," *Phys. Rev. Lett.*, vol. 85, pp. 4992–4995, 2000.
- [5] A. J. Storm, J. van Noort, S. de Vries, and C. Dekker, "Insulating behavior for DNA molecules between nanoelectrodes at the 100 nm length scale," *Appl. Phys. Lett.*, vol. 79, pp. 3881–3883, 2001.
- [6] M. Bockrath, N. Markovic, A. Shepard, M. Tinkham, L. Gurevich, L. P. Kouwenhoven, M. S.-W. Wu, and L. L. Sohn, "Scanned conductance microscopy of carbon nanotubes and λ -DNA," *Nano Lett.*, vol. 2, pp. 187–190, 2002.
- [7] B. Q. Xu, P. Zhang, X. Li, and N. J. Tao, "Direct conductance measurement of single DNA molecules in aqueous solution," *Nano Lett.*, vol. 4, pp. 1105–1108, 2004.
- [8] K. Keren, M. Krueger, R. Gilad, G. Ben-Yoseph, U. Sivan, and E. Braun, "Sequence-specific molecular lithography on single DNA molecules," *Science*, vol. 297, pp. 72–75, 2002.
- [9] M. Adachi, K. Mori, Y. Sato, and L. Pei, "Gold nanowire formation of 2-dimensional network structure with electric conductivity," *J. Chem. Eng. Jpn.*, vol. 37, pp. 604–608, 2004.
- [10] K. Keren, R. S. Berman, and E. Braun, "Patterned DNA metallization by sequence-specific localization of a reducing agent," *Nano Lett.*, vol. 4, pp. 323–326, 2004.
- [11] H. A. Becerril, R. M. Stoltenberg, C. F. Monson, and A. T. Woolley, "Ionic surface masking for low background in single- and double-stranded DNA-templated silver and copper nanorods," *J. Mater. Chem.*, vol. 14, pp. 611–616, 2004.
- [12] C. F. Monson and A. T. Woolley, "DNA-templated construction of copper nanowires," *Nano Lett.*, vol. 3, pp. 359–363, 2003.
- [13] W. E. Ford, O. Harnack, A. Yasuda, and J. M. Wessels, "Platinated DNA as precursors to templated chains of metal nanoparticles," *Adv. Mater.*, vol. 13, pp. 1793–1797, 2001.
- [14] R. Seidel, M. Mertig, and W. Pompe, "Scanning force microscopy of DNA metallization," *Surf. Interface Anal.*, vol. 33, pp. 151–154, 2002.
- [15] J. Richter, R. Seidel, R. Kirsch, M. Mertig, W. Pompe, J. Plaschke, and H. K. Schackert, "Nanoscale palladium metallization of DNA," *Adv. Mater.*, vol. 12, pp. 507–510, 2000.
- [16] J. Richter, M. Mertig, W. Pompe, I. Mönch, and H. K. Schackert, "Construction of highly conductive nanowires on a DNA template," *Appl. Phys. Lett.*, vol. 78, pp. 536–538, 2001.
- [17] J. Richter, M. Mertig, W. Pompe, and H. Vinzelberg, "Low-temperature resistance of DNA-templated nanowires," *Appl. Phys. A*, vol. 74, pp. 725–728, 2002.
- [18] Z. Deng and C. Mao, "DNA-templated fabrication of 1D parallel and 2D crossed metallic nanowire arrays," *Nano Lett.*, vol. 3, pp. 1545–1548, 2003.
- [19] S. Yoda, S. P. Han, H. Kudo, K. J. Kwak, and M. Fujihira, "Deoxyribonucleic acid interaction with silanized surfaces," *Jpn. J. Appl. Phys.*, vol. 43, pp. 6297–6302, 2004.
- [20] X. Michalet, R. Ekong, F. Fougerousse, S. Rousseaux, C. Schurra, N. Hornigold, M. van Slegtenhorst, J. Wolfe, S. Povey, J. S. Beckmann, and A. Bensimon, "Dynamic molecular combing: Stretching the whole human genome for high-resolution studies," *Science*, vol. 277, pp. 1518–1523, 1997.
- [21] S. P. Han, S. Yoda, K. J. Kwak, K. Suga, and M. Fujihira, "Interpretation of DNA adsorption on silanized surfaces by measuring interaction forces at various pHs using atomic force microscopy," *Ultramicroscopy*, vol. 105, pp. 148–154, 2005.
- [22] H. Kind, M. Geissler, H. Schmid, B. Michel, K. Kern, and E. Delamarche, "Patterned electroless deposition of copper by microcontact printing palladium(II) complexes on titanium-covered surfaces," *Langmuir*, vol. 16, pp. 6367–6373, 2000.
- [23] A. M. T. van der Putten, "Controlled mechanical adhesion of electroless Cu patterns," *J. Electrochem. Soc.*, vol. 140, pp. 2376–2377, 1993.
- [24] J.-R. Henry, "Electroless (autocatalytic) plating," *Met. Finish.*, vol. 100, pp. 409–420, 2002.
- [25] T. A. Brown, *Genomes*, 2nd ed. Oxford, U.K.: BIOS Scientific, 2002.



Hidetoshi Kudo received the B.E. and M.E. degrees in biomolecular engineering from the Tokyo Institute of Technology, Tokyo, Japan, in 2002 and 2004, respectively, and is currently working toward the Ph.D. degree at the Tokyo Institute of Technology.



Masamichi Fujihira received the B.Eng. degree in applied chemistry from Yokohama National University, Yokohama, Japan, in 1966, and the Dr.Eng. degree in industrial chemistry from The University of Tokyo, Tokyo, Japan, in 1971.

In April 1971, he joined the Institute of Solid State Physics, The University of Tokyo, as a Research Associate and in August 1972, he joined the Department of Chemistry, The Ohio State University, Columbus, as a Visiting Research Associate. In March 1974, he joined the Institute of Industrial Science, The University of Tokyo, as an Assistant. In July 1975, he joined the Pharmaceutical Institute, Tohoku University, Sendai, Japan, as a Lecturer and, in July 1976, was promoted to an Associate Professor with the same institute. In April 1983, he joined the Department of Chemical Engineering, Tokyo Institute of Technology, Tokyo, Japan, as an Associate Professor, was promoted to Professor with the same department in March 1986, and, since April 1988, has been with the Department of Biomolecular Engineering as a Professor. His current research interests include single molecular devices, organic light-emitting diodes, organic photovoltaic cells, nanocontact printing, novel nanofabrication, and various scanning probe microscopies such as scanning tunneling microscopy, friction force microscopy, scanning near-field optical microscopy, Kelvin probe force microscopy, adhesive force mapping with pulse force mode atomic force microscopy (AFM), and noncontact AFM.

8 Fabrication, Characterization and Physical Properties of Nanostructured Metal Replicated Membranes

Yong Lei*, Weiping Cai and Lide Zhang
*Institute of Solid State Physics, Chinese Academy of Sciences,
Hefei 230031, People's Republic of China*

1 INTRODUCTION

As a well-known host, highly ordered anodic alumina membranes (AAMs) have been playing an important role in the fabrication of many kinds of nanowires (Lei *et al.*, 2001) and nanotubes (Hulteen and Martin, 1998). However, the AAMs have some disadvantages in actual use such as the insufficient chemical and thermal stability, together with the low mechanical strength. Moreover, the AAM itself is an insulator. Therefore, it is worth studying how to fabricate highly ordered metal (Masuda and Fukuda, 1995) or semiconductor membranes (Hoyer *et al.*, 1995) with attractive chemical and physical properties.

Recently, highly ordered metal (Co and Ni) replicated membranes (MRM) were fabricated by a novel replicating method in our lab (Lei *et al.*, 2001). We used some new techniques to replicate the MRMs from the AAMs, such as the immersion of the AAM in methyl methacrylate (MMA) monomer, pre-polymerization of MMA, and four-directional evaporation of Pd catalyst. These new techniques lead to a full replication of the AAM and result in an almost ideally arranged nanohole array of the replicated MRM with the following features: high aspect ratio of more than 320, highly ordered pore arrays, narrow size distributions of pore diameters. Moreover, the overall fabrication process of MRMs was greatly simplified.

After the magnetic measurement to the MRMs, we found out that they have some novel magnetic properties due to their special nanostructures. The most desirable is their unusual preferred magnetization direction. Different from many usual magnetic films, the preferred magnetization direction of the metal membranes (both in Co and Ni membranes) is perpendicular to the membrane plane, which is valuable to be used in perpendicular magnetic recording systems.

* Corresponding author, now is a Visiting Scholar in National University of Singapore. Email address: yuanzhilei@yahoo.com, smaleiy@nus.edu.sg.

2 FABRICATION AND MAGNETIC PROPERTIES

Fig. 1 summarizes our preparation procedure in a schematic manner. After the preparation of the through-hole AAM [(a)-(d)], a very thin Pd catalyst layer was deposited on the surface of it by using a four-directional evaporation method to improve the distribution regularity of the catalyst on the surface [(e)]. The AAM was then immersed into the MMA monomer followed by the pre-polymerization and polymerization of MMA [(f)-(g)], that resulted in a PMMA cylindrical array with Pd catalyst located at the root of the PMMA cylinders [(h)]. Finally, the electroless deposition was carried out at the catalyst site [(h)-(i)], forming double-sided and single-sided MRMs by changing the deposition times. The MRMs have a very good regularity of the pore arrangement [Figs. 2(a) and (b)] and is almost identical to that of the original mother membranes – AAMs, but most important is that the pore arrays of the MRMs have a very high aspect ratio of about 320, which is a great improvement in this field.

It is well known that all the ferromagnetic materials, such as Co and Ni, have anisotropic magnetic properties. For a ferromagnetic thin film, because the demagnetizing factors are about 0 and 4π for fields parallel and perpendicular to the film plane, the shape anisotropy tends to force the magnetization M to be in the film plane, resulting in a preferred magnetization direction parallel to the film plane. However, it is highly desirable, particularly in perpendicular magnetic recording systems, to have M perpendicular to the film. Many attempts have been done to overcome the difficulty; the most successful is the metallic nanowire arrays prepared by Whitney *et al.* (1993). But this kind of magnetic film is actually not a continuous film and should have some confinement in application.

We carried out the measurement of the magnetic hysteresis loop to both the Co and Ni MEMs [Fig. 3]. The Ni MEM has a preferred magnetization direction perpendicular to the film plane both in 5 K and 300 K [Figs. 3(a) and (b)]. Also, we fabricated a normal compact Co film by using the same electroless deposition process as that of the Co MEM. It can be seen that this Co film has a preferred direction parallel to the film [Fig. 3(c)] while the Co MEM has a perpendicular preferred direction [Fig. 3(d)].

This unusual preferred magnetization direction of the MEMs should originate from their unique nanoporous structure, in some ways like that of the magnetic metallic arrays. The pore walls of the MEM are composed of very small nanoparticles with diameters of about 10 nm; also they have configuration with a high aspect ratio along the pore axis, forming a highly anisotropic structure in nanometer scale. In the magnetization process, this anisotropic structure should force the domain wall to move along the perpendicular direction of the pore wall, thus cause the domain to extend along the same direction. All these will result in a preferred magnetization direction along the pore axis, which is the same direction as that perpendicular to the MEM film plane.

The new features and the novel magnetic properties of the MRMs should lead to a potential technological and scientific application in many fields, including magnetic recording system, electrodes and sensor devices.

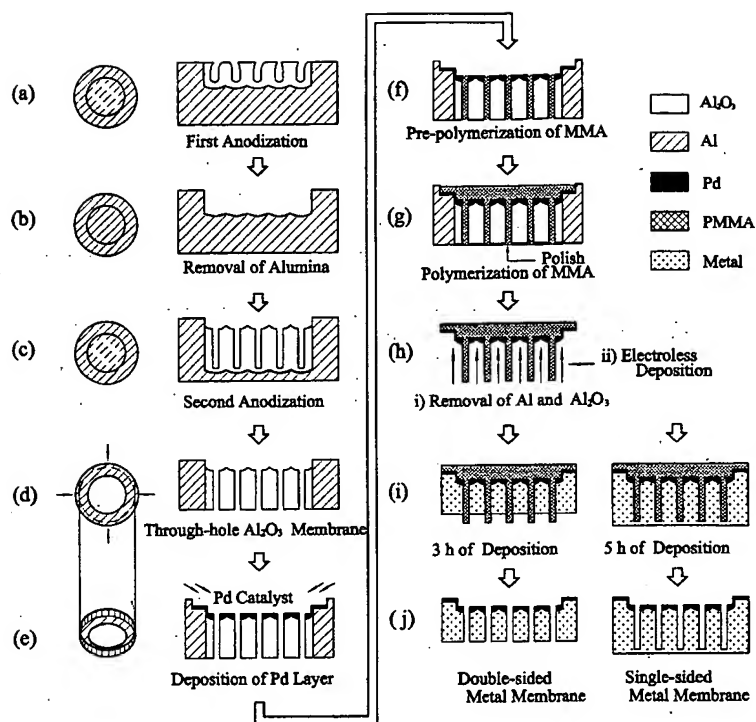


Figure 1 Schematic Diagram of the fabrication of highly ordered nanoporous metal membranes.

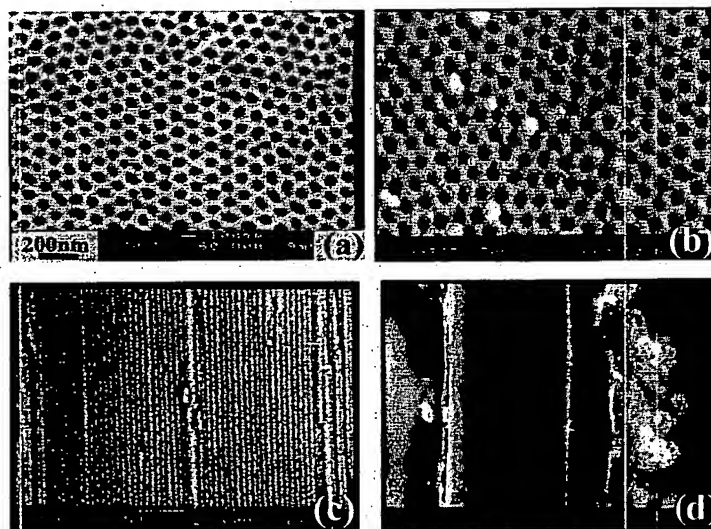


Figure 2 SEM images of the highly ordered metal membranes: top view of the Ni membrane (a) and the Co membrane (b), partial (c) and entire (d) cross section view of the Co membrane.

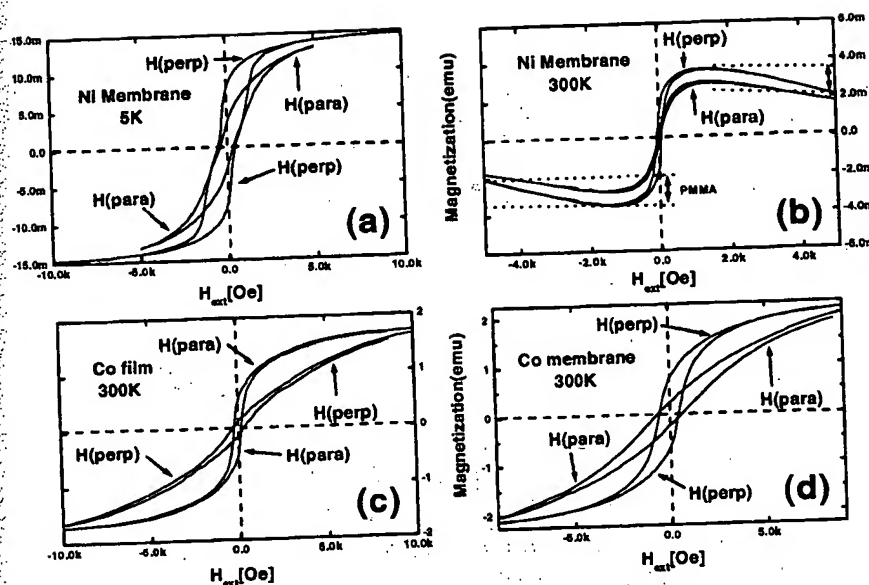


Figure 3 The magnetization hysteresis loops with the magnetic field applied parallel and perpendicular to the membrane (or film) planes: Ni nanoporous membranes measured at 5 K (a) and 300 K (b); a normal compact Co film prepared by the same electroless deposition as that of the Co nanoporous membrane (c), measured at 300 K; Co nanoporous membranes measured at 300 K (d).

REFERENCES

- Hoyer, P., Baba, N. and Masuda, H., 1995, Small quantum-sized CdS particles assembled to form a regularly nanostructured porous film, *Applied Physics Letters*, **66**, pp. 2700-2702.
- Hulteen, J.C. and Martin, C.R., 1998, Template synthesis of nanoparticles in nanoporous membranes, In *Nanoparticles and Nanostructured Films*, Chapter 10, edited by Fendler, J.H., (Berlin: Wiley-Vch), pp. 235-262.
- Lei, Y., Liang, C.H., Wu, Y.C., Zhang, L.D. and Mao, Y.Q., 2001, Preparation of highly ordered nanoporous Co membranes assembled by small quantum-sized Co particles, *Journal of Vacuum Science and Technology B*, **19**, pp. 1109-1114.
- Lei, Y., Zhang, L.D., Meng, G.W., Li, G.H., Zhang, X.Y., Liang, C.H., Chen, W. and Wang, S.X., 2001, Preparation and photoluminescence of highly ordered TiO₂ nanowire arrays, *Applied Physics Letters*, **78**, pp. 1125-1127.
- Masuda, H. and Fukuda, K., 1995, Ordered metal nanohole arrays made by a two-step replication of honeycomb structures of anodic alumina, *Science*, **268**, pp. 1466-1468.
- Whitney, T.M., Jiang, J.S., Searson, P.C. and Chien, C.L., 1993, Fabrication and magnetic properties of arrays of metallic nanowires, *Science*, **261**, pp. 1316-1319.

Nano Science and Technology: Novel Structures and Phenomena

Edited by

Zikang Tang and Ping Sheng

*Hong Kong University of Science and Technology
Clear Water Bay, Hong Kong*



Taylor & Francis
Taylor & Francis Group
LONDON AND NEW YORK

First published 2003
by Taylor & Francis
11 New Fetter Lane, London EC4P 4EE

Simultaneously published in the USA and Canada
by Taylor & Francis Inc,
29 West 35th Street, New York, NY 10001

Taylor & Francis is an imprint of the Taylor & Francis Group

© 2003 Zikang Tang and Ping Sheng

Printer's Note:

This book was prepared from camera-ready-copy
supplied by the authors

Printed and bound in Great Britain by
TJ International, Padstow, Cornwall

All rights reserved. No part of this book may be reprinted or
reproduced or utilised in any form or by any electronic,
mechanical, or other means, now known or hereafter
invented, including photocopying and recording, or in any
information storage or retrieval system, without permission in
writing from the publishers.

Every effort has been made to ensure that the advice and information
in this book is true and accurate at the time of going to press.
However, neither the publisher nor the authors can accept any legal
responsibility or liability for any errors or omissions that may be made.
In the case of drug administration, any medical procedure or
the use of technical equipment mentioned within this book,
you are strongly advised to consult the manufacturer's guidelines.

British Library Cataloguing in Publication Data

A catalogue record for this book is available from the British Library

Library of Congress Cataloging in Publication Data

Croucher ASI on Nano Science and Technology (2nd : Hong Kong
University of Science and Technology)

Nano science and technology : novel structures and
phenomena / edited by Zikang Tang and Ping Sheng.
p. cm.

Proceedings of the second Croucher ASI on Nano Science and Technology,
held at the Hong Kong University of Science and Technology
Includes bibliographical references and index.

ISBN 0-415-30832-1 (hb)

1. Nanostructure materials—Congresses. 2. Nanotechnology—Congresses.
I. Tang, Zikang, 1959– II. Sheng, Ping, 1946– III. Title.

TA418.9.N35 C76 2003
620'.5—dc21

2002075066

ISBN 0-415-30832-1



Fabrication and thermal annealing behavior of nanoscale ripple fabricated by focused ion beam

D.Z. Xie*, B.K.A. Ngoi, W. Zhou, Y.Q. Fu

*Precision Engineering and Nanotechnology Center, School of Mechanical and Production Engineering,
Nanyang Technological University, Nanyang Avenue, Singapore 639798, Singapore*

Received 25 October 2003; received in revised form 28 November 2003; accepted 28 November 2003

Abstract

The development, during annealing, of periodic one-dimensional ripple structure has been investigated. The nanoscale ripple array was fabricated on silicon(0 0 1) crystal surface using focused ion beam (FIB). Annealing was performed isothermally in a flowing argon gas ambient at 670 °C. The morphology of the ripple before and after annealing was analyzed by use of atomic force microscope. The height of the ripple decreased after thermal annealing. Furthermore, after annealing, spikes of gallium and/or gallium-rich precipitate were also observed on the surface of the ripples and the FIB milled areas.

© 2003 Elsevier B.V. All rights reserved.

PACS: 68.35Bs; 79.20Rf

Keywords: Focused ion beam; Sputtering; Micromachining; Surface diffusion

1. Introduction

Nanostructuring and nanofabrication is continuously growing in many areas [1–3]. As the feature size of devices has been reduced to a submicrometer or nanometer scale, e.g., the feature size of Si IC chip has been shrunk to a point less than 100 nm, the thermal stability of the nanoscale structure has been being a great concern [4–8]. Keefe et al. (KUB) [6] studied the annealing behavior of periodic atomic step arrays associated with etched sinusoidal grating structures on Si(0 0 1). In their experiments the grating wavelengths (4–6 μm) are in micrometer scale, and the amplitudes (~100 nm) are in the nanoscale. They

used lithographic technique to produce these sinusoidal patterns and used STM to monitor the development of the periodic grating. They found that the grating amplitudes decay exponentially with time in the temperature range from 800 to 1100 °C. Erlebacher et al. [4] studied nanometer scale ripples (both period and amplitude are in nanometer scale) and observed a nonexponential decay for the time evolution of the ripple amplitude during anneals over the temperature range 650–750 °C. In their experiment the periodic ripple structures were made on Si(0 0 1) by sputter rippling, i.e. the ripple self assembled during low energy Ar⁺ ion bombardment at glancing angles and elevated temperatures.

The focused ion beam (FIB) is now an indispensable tool in both nanoscale characterization and fabrication of electronic materials and devices [1,9–11]. FIBs have had a great impact on the technology of

* Corresponding author. Tel.: +65-67906875;
fax: +65-67904674.
E-mail address: dzxie6470@hotmail.com (D.Z. Xie).

integrated circuit fabrication. It is one of main tools for failure analysis of integrated circuit by cutting of wires to isolate elements of a circuit or connecting electrically isolated elements with wires created by the deposition of metals [12]. It has also been used to fabricate high density optical storage [13] and high density magnetic storage [14]. FIB deposition of nanointerconnects (NIs) is an attractive approach to the formation of electrical contacts to structures such as carbon nanotubes and single molecules [15]. In recent years, FIBs have been used to investigate the ripple formation [16,17]. It has the advantage to observe in situ the formation progress of ripple structure by detecting the secondary electrons emitted from the surface during FIB etching.

In this paper we report the experimental observation of morphology of nanoscale rippled surface before and after thermal annealing. In our research, we used FIB to fabricate the one-dimensional periodic nanoscale ripple grating on Si(0 0 1) surface. Using of FIB direct writing methods the period of the grating can be very easily controlled.

2. Experiment

In this work, the fabrication of ripple was accomplished by using a Micrion Workstation 9500EX. This FIB system uses gallium ions (Ga^+) which can be accelerated up to a highest energy of 50 keV after their extraction from a liquid metal ion source (LIMS). The ion beam energy used in this work was 45 keV, the extraction current was about 2.5 μA . The limiting aperture size was 25 μm and the focused ion beam current was 10–20 pA, yielding a beam diameter of approximately 20–25 nm (full width at half maximum, i.e., FWHM). The chamber pressure was 1.65×10^{-7} Torr during etching process. The ion beam is normally incident on the sample surface. Each periodic grating is defined in a $5 \mu\text{m} \times 6 \mu\text{m}$ area including 10 ripples that were fabricated one by one. The grating period is designed to be 600 nm. The amplitude of the ripple ranges from 20 to 100 nm. And the width of the ripple ranges from 40 to 140 nm. After FIB etching and subsequently isothermal annealing, the ripple gratings were measured using a Digital Instruments Nanoscope III multimode atomic force microscopy (AFM) in tapping mode.

The isothermal annealing was performed in flowing high purity argon (Ar) gas at 670 °C for 3000 s using Nabertherm R40/250/12-C6 furnace. Prior to annealing the sample, a flow of 45 sccm Ar gas was introduced into the furnace for 10 min to blow away the air. During annealing the flow rate of Ar gas was kept 10 sccm.

3. Result and discussion

In our experiments three groups of ripple gratings have fabricated. Each ripple grating consists of 10 ripples in a $5 \mu\text{m} \times 6.6 \mu\text{m}$ area. The 10 ripples were defined by etching 11 box one by one with a pitch of 0.6 μm . The details of the designed parameters are listed in Table 1. Fig. 1 shows the AFM image of ripple grating A(1). According to the AFM results the height of the ripple, after milling, depends to the ripple width. Fig. 2 shows the dependence of the ripple height on its width. From Fig. 2 it can be seen that for 40 nm width ripple grating A(1) the residue height (8.9 nm) is much smaller than the designed height (20 nm) due to milling down of the whole area. For the 140 nm width ripple grating C(1) the experimental ripple height (21.3 nm) is a little higher than the designed height (20 nm), i.e. the apex of the ripple is a little higher than the unetched surface. It can be seen from Figs. 1 and 2 that the edges of the grating are also higher than the unetched area. Two factors are contributed to this extruding. The first is due to the beam tail effects. Since the distribution of the ion beam intensity is Gaussian shape. The low intensity of beam tail will cause the substrate damaged or amorphization at the defined box edges [18]. As the damaged and amorphous material has a lower density than the crystalline one, a swelling of the sample surface at the box rim

Table 1
Designed parameters of the ripple gratings

Width (nm)	Height (nm) ($i = 1-5$)				
Group A (40)	20	40	60	80	100
Group B (90)	20	40	60	80	100
Group C (140)	20	40	60	80	100

The period is 0.6 μm for all gratings.

The designed height is expected to equal the depth estimated by the dose dependence of etched depth, i.e., $3.6 \text{ nC}/\mu\text{m}^2$ ion dose corresponds to 1 μm etched depth.

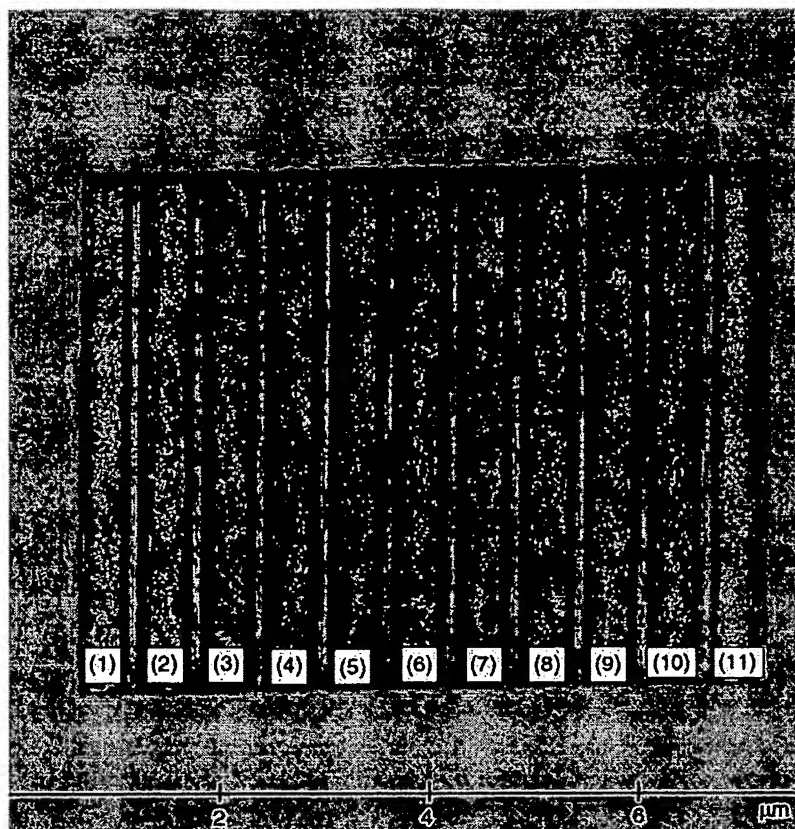


Fig. 1. A two-dimensional top view image of ripple grating A(1) measured by AFM to show the fabrication process and morphology, in which the 10 ripples were fabricated one by one as the sequence labeled in the image.

can be expected [19]. The second is the redeposition. When the ion beam was scanning at the defined box edge, some of the sputtered substrate atoms would redeposit on the surface most nearby the defined box.

Fig. 3 displays the dependence of experimental height on the designed width of ripple. It can be seen that the narrower the ripple is, the larger the difference between designed height and experimental height. For grating group A, after reaching about 31 nm, the ripple height will not increase as the etched depth increases. For group C, the experimental heights are nearly equal to the designed values. On the other hand, the experimental width (full width at half maximum, i.e., FWHM) of the ripple increases as the etched depth increases, except for group A. For group A, the average width of the ripples in all five gratings are 205 nm. In groups B and C the width of the ripple

increases as the ripple height increases. Fig. 4 is the experimental results of group C, the line is used as a guide to eyes.

In order to investigate the annealing behavior of the nanoscale ripple, the sample with ripple gratings was annealed in flowing Ar gas at 670 °C. Smoothing of the ripples has been observed after 3000 s annealing. Figs. 5 and 6 show two AFM images of annealed grating. From these two images it can be seen that the ripples do not obviously emerge. At some places the ripple almost completely vanished. The average height of ripples after annealing depends on the ripple width before annealing. For annealed gratings the height of ripples was measured at the place where there is no spike. R_{ave} (defined as the ratio of average height of the ripples in a grating after annealing to the average height of that ripples before annealing) is 0.63 for all of the five gratings in group A. For gratings in

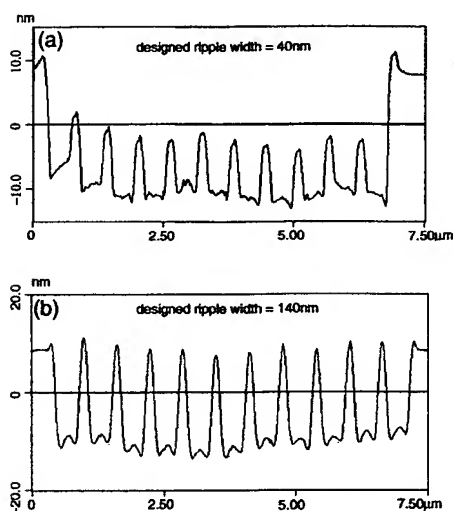


Fig. 2. Height profile (from AFM image) of grating A(1) and C(1) to display effect of ripple width to its height. Ripple heights in both gratings are designed to be 20 nm.

groups B and C, the R_{ave} ranges between 0.64–0.78 and 0.64–0.85, respectively.

From Figs. 5 and 6, it can be seen that there are many granular spikes in the grating area. Fig. 5B clearly shows that some of the spikes are even much higher than the milled depth. These granular spikes can be assumed to be gallium and/or Ga-rich precipitates formed during annealing due to precipitation of the implanted gallium [20]. During FIB milling the gallium ions were implanted into the subsurface of the substrate. The surface layer became amorphous due to

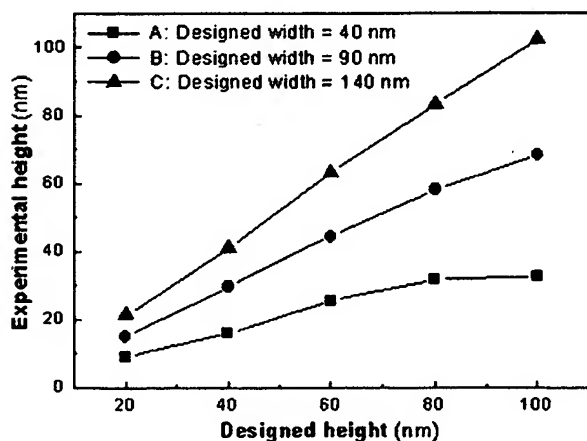


Fig. 3. Comparison of designed heights and experimental heights for different width ripples.

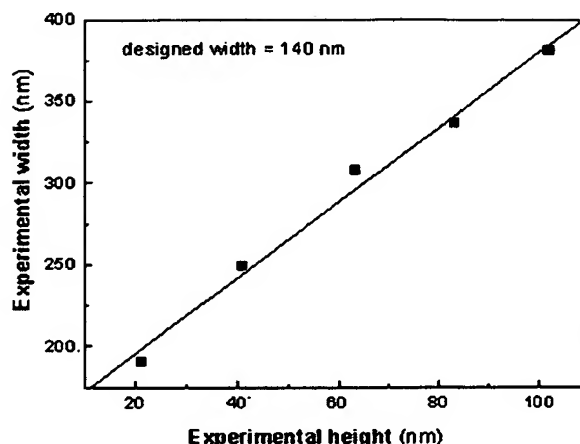


Fig. 4. Relation between ripple width and height for group C gratings.

the Ga ion implantation and some of the surface material were sputtered off. As a result of sputtering and implantation, the Ga concentration in the surface region increases with the milled depth. According to

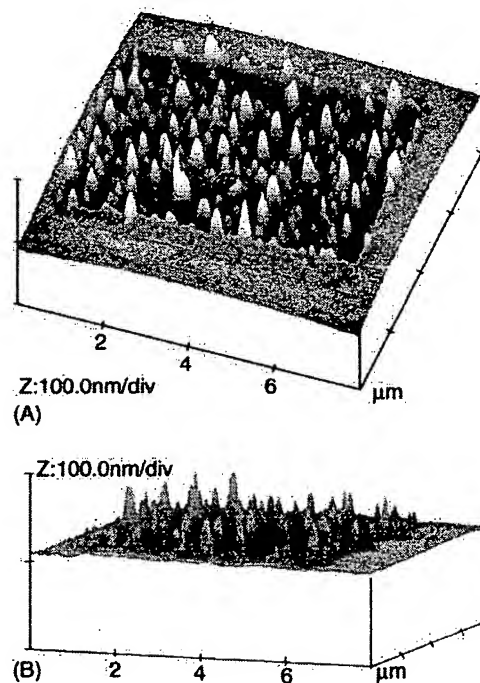


Fig. 5. Three-dimensional AFM images to reveal the morphology of the ripple grating A(1) after annealing in flowing of Ar gas at 670 °C for 3000 s.

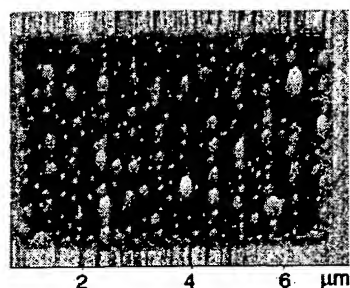


Fig. 6. AFM image of the grating B(1) showing the preferential site of the precipitates after annealing in flowing of Ar gas at 670 °C for 3000 s.

TRIM 2000 code simulation the project range is 36.6 nm with 13.1 nm straggle for 45 keV gallium ions. This means the maximum concentration lies at a depth of approximately 36.6 nm for low dose. After removing of about 20 nm material, the surface Ga concentration reaches a saturation value of about 12% of Si atom density in substrate [18]. During thermal annealing the amorphous layer of the sample recrystallized from the interface of crystalline substrate and amorphous surface layer toward the surface. The crystallization front will drive the implanted gallium atoms out of solution. The implanted Ga moved toward the surface, precipitated and assembled into spikes at the surface [21]. Meanwhile some gallium evaporated from the surface into the flowing Ar atmosphere. Most of the gallium and/or Ga-rich precipitates are located at surface of the ripple or nearby the ripples, as shown in Figs. 5 and 6. This means that the convex maybe a preferential site for the aggregation of gallium. The precipitation of gallium during heat treatment should be a significant factor of concerns for micro device fabrication processes which including FIB micromachining or deposition using gallium as ion source and high temperature heat treatment.

In Erlebacher's experiments [4] for the ripples with average height = 20 nm and period = 565 nm (this period is close to our grating period 600 nm) created by Ar ion beam etching, the R_{ave} was about 0.31 after annealing at 672 °C for 3000 s in a clean ultrahigh vacuum. This value is much smaller than ours. Since implanted Ga has a remarkable influence on the diffusion of impurities in Si during annealing [21]. Therefore we assume that the gallium would also has an influence on the surface diffusion of Si atoms due to

the precipitation of implanted gallium at the surface during the annealing.

4. Conclusion

The following main conclusion may be made. Smoothing of nanoscale ripple fabricated by FIB has been observed after annealing. The implanted gallium diffuses toward the surface and precipitates at the surface during annealing. The convex is a preferential site for aggregation of gallium.

References

- [1] H. Namatsu, Y. Watanabe, K. Yamazaki, T. Yamaguchi, M. Nagase, Y. Ono, A. Fujiwara, S. Horiguchi, *J. Vac. Sci. Technol. B* 21 (2003) 1.
- [2] D.M. Longo, W.E. Benson, T. Chraska, R. Hull, *Appl. Phys. Lett.* 78 (2001) 981.
- [3] F.J. Martin, C. Grove, *Biomed. Microdevice* 3 (2) (2001) 97.
- [4] J. Erlebacher, M.J. Aziz, E. Chason, M.B. Sinclair, J.A. Floro, *Phys. Rev. Lett.* 84 (2000) 5800.
- [5] N.C. Bartelt, W. Theis, R.M. Tromp, *Phys. Rev. B* 54 (1996) 11741.
- [6] M.E. Keeffe, C.C. Umbach, J.M. Blakely, *J. Phys. Chem. Solids* 55 (1994) 965.
- [7] S. Tanaka, N.C. Bartelt, C.C. Umbach, R.M. Tromp, J.M. Blakely, *Phys. Rev. Lett.* 78 (1997) 3342.
- [8] M. Ozdemir, A. Zangwill, *Phys. Rev. B* 45 (1991) 3718.
- [9] S. Matsui, Y. Ochiai, *Nanotechnology* 7 (1996) 247.
- [10] D.N. Dunn, R. Hull, *Appl. Phys. Lett.* 75 (1999) 3414.
- [11] J. Voigt, F. Shi, P. Hudek, I.W. Rangelow, K. Edinger, *J. Vac. Sci. Technol. B* 18 (2000) 3525.
- [12] J. Orloff, *Rev. Sci. Instrum.* 64 (1993) 1105.
- [13] B.K. Lee, C.J. Chi, I. Chyr, S.D. Lee, F.R. Beyette, A.J. Steckl, *Opt. Eng.* 41 (2002) 742.
- [14] J. Lohau, A. Moser, C.T. Rettner, M.E. Best, B.D. Terris, *Appl. Phys. Lett.* 78 (2001) 990.
- [15] J.-F. Lin, J.P. Bird, L. Rotkina, P.A. Bennett, *Appl. Phys. Lett.* 82 (2003) 802.
- [16] A. Datta, Y.-R. We, Y.L. Wang, *Phys. Rev. B* 63 (2001) 125407.
- [17] S. Habenicht, K.P. Lieb, J. Koch, A.D. Wieck, *Phys. Rev. B* 65 (2002) 115327.
- [18] C. Lehrer, L. Frey, S. Petersen, H. Ryssel, *J. Vac. Sci. Technol. B* 19 (2001) 2533.
- [19] B. Basnar, A. Lugstein, H. Wanzenboeck, H. Langfischer, E. Bertagnolli, E. Gornik, *J. Vac. Sci. Technol. B* 21 (2003) 927.
- [20] A. Lugstein, B. Basnar, E. Bertagnolli, *J. Vac. Sci. Technol. B* 20 (2002) 2238.
- [21] K. Yokota, H. Furuta, S. Ishihara, I. Kimura, *J. Appl. Phys.* 68 (1990) 5385.

Fabrication of silicon cones and pillars using rough metal films as plasma etching masks

K. Seeger^{a)} and R. E. Palmer

Nanoscale Physics Research Laboratory, School of Physics and Astronomy, The University of Birmingham, Edgbaston, Birmingham B15 2TT, United Kingdom

(Received 13 November 1998; accepted for publication 20 January 1999)

We have developed a simple fabrication process which allows the production of nanoscale silicon structures. Rough silver films are used as an etching mask for reactive ion etching at 10 °C. Variation of the etching parameters, such as the rf power, allows control over the shape of the features; the production of both pillars and cones is possible. The density and diameter of these features are controlled by the etching time. Pillars with diameters as small as 5 nm are reported.
© 1999 American Institute of Physics. [S0003-6951(99)02911-3]

The production of silicon structures on the nanometer scale has attracted much interest in the last decade, because of distinctive differences in the properties of these nanostructures compared with the bulk material. One key example is the emission of visible light first reported by Canham.¹ In consequence, considerable efforts are under way to develop fabrication processes which allow the production of these structures in order to investigate their optical² and electronic properties.³ A further aim of this research is to integrate the nanoscale Si material into electronic devices,⁴ which take advantage of the novel properties. For technological applications, the more straightforward the fabrication scheme the better, so "simple" processes are highly desirable.

Several groups have developed processes to produce silicon pillars with diameters in the nanometer range.^{5–11} A standard method is the use of lithographic techniques. One problem with this approach is the limited resolution of optical lithography, a problem which can be overcome by using electron-beam (*e*-beam) lithography at high energies, i.e., shorter wavelength. Through the use of special resists, pillars and other structures with dimensions of below 10 nm have been produced by *e*-beam lithography.^{5,6} Another possible route to produce sub-10 nm silicon pillars is the application of lithographic techniques with a subsequent thinning of the structures by HF wet etching.⁷ Nassiopoulou *et al.*⁸ produced 50 nm structures with deep ultraviolet (UV) lithography and plasma etching techniques, and the thinning of the pillar diameter was achieved by thermal oxidation followed by a wet etch process. The pillars produced with this process have a diameter below 10 nm and exhibit visible luminescence.⁹ In a previous report we describe the production of silicon pillars with diameter of around 10 nm using size-selected clusters as etch masks.^{10,11} An electron cyclotron resonance (ECR) etching process was performed at –130 °C, the masking behavior is based on the condensation of reaction products on the clusters, which act as nucleation sites. Consequently, the pillar diameter depends on the cluster material but not on the cluster size. The fabrication of silicon cones is also of great interest, e.g., for the development of electron field-emitting devices.^{12,13} The conical shape can be obtained by preparing

masks with lithographic techniques and then etching the samples isotropically, so that undercut of the resist occurs, which results in the formation of silicon tips.^{14,15}

The process which we report in this letter employs rough silver films as etching masks. The films are deposited onto a Si(111) wafer with a magnetron sputter coater system (Auto 306, Edwards). Silver is known to grow on this substrate for higher coverages via the formation of three-dimensional islands rather than in a layer by layer mode.¹⁶ This leads to the growth of a rough film containing silver clusters, shown in Fig. 1. This picture of a silver film with mean thickness of around 20 nm was taken with an atomic force microscope (AFM). The silver clusters forming the film have a typical diameter of 20–40 nm. After film deposition the samples are etched in a reactive ion etching (RIE) system (Plasmalab 80 Plus, Oxford Instruments) with SF₆ and CF₄ as etching gases. Etching of silicon with SF₆ at room temperature is known to result in isotropic etching,¹⁷ but a mixture of these two gases leads to anisotropic etching arising from polymer deposition on the sidewalls of the pillars, which inhibits undercut of the masks.^{18,19} The gases are used in a ratio of 1:1 at a total flow rate of 50 sccm and a pressure of 6 mTorr. The temperature during the etching process was usually kept constant by water cooling at 10 °C.^{20,21} The rf power was varied from 200 W, which induced a self-bias on the sample of –624 V, to 50 W (self-bias –243 V).

Figure 2 is a schematic of the fabrication process. After

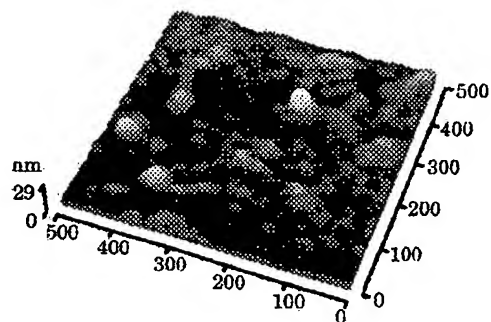


FIG. 1. Atomic force micrograph of a rough silver film sputtered onto a Si(111) wafer. The average film thickness is approximately 20 nm.

^{a)}Electronic mail: katrin@nprl.ph.bham.ac.uk

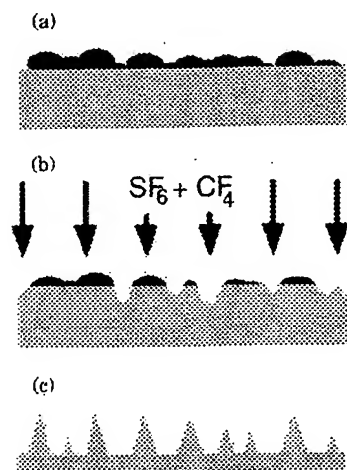


FIG. 2. Schematic of the fabrication process. (a) A rough silver film is deposited on the substrate. (b) The plasma reduces the size of the silver islands by sputtering, exposing regions of the silicon surface to the etching gas. (c) After the etching process silicon cones are produced.

deposition of the rough silver film, Fig. 2(a), the sample is etched using the plasma process described above. First, the silver film is sputtered by the ions formed in the plasma, leaving separated, monodispersed silver islands on the substrate. When the plasma reaches the silicon surface, chemical etching of the substrate begins, prevented only at areas where silver islands are still present, Fig. 2(b). During the etching process the silver islands are reduced in size by sputtering, which leads to the formation of silicon cones, Fig. 2(c).

Figure 3 shows scanning electron micrographs of the silicon structures produced at different etching powers. In this case the rf power was varied from 200 to 50 W, the examples shown correspond to 200 W [Fig. 3(a)], 150 W [Fig. 3(b)], and 100 W [Fig. 3(c)]. At high etching powers, e.g., 200 W, silicon cones are formed. A detailed analysis [Fig. 3(d)] shows that the angle at the apex of the cones produced at 200 W lies in the range from 20° to 45° , while at 120 W the sides are much steeper, with cone angles from 8° to 30° . Typical radii of the cone tips are 10 nm. At lower etching powers of about 100 W, straight pillars are formed which still have silver islands on top [Fig. 3(c)]. An etching power below 80 W did not allow efficient sputtering of the silver film, so it was not possible to form silicon pillars at these low powers.

The likely mechanism for the behavior observed is as follows. At a high rf power (i.e., high sample bias) the silver islands are reduced in size as etching proceeds, thus exposing areas of the substrate which were previously protected. This creates a conical shape of the structure. At 100 W the sputter rate for silver is much lower, i.e., islands remain much longer on the surface and protect the underlying area. Pillars with straight sidewalls are formed instead of cones. Thus, in effect, the ratio of the speeds of the two processes, (i) physical sputtering of the silver film and (ii) (anisotropic) chemical etching of the silicon substrate, determines whether the etching leads to cone or pillar formation. The capacity to control the shape of the silicon nanostructures produced simply through choice of rf power is, of course, a very attractive aspect of the method.

Downloaded 14 Aug 2005 to 130.207.165.29. Redistribution subject to AIP license or copyright, see <http://apl.aip.org/apl/copyright.jsp>

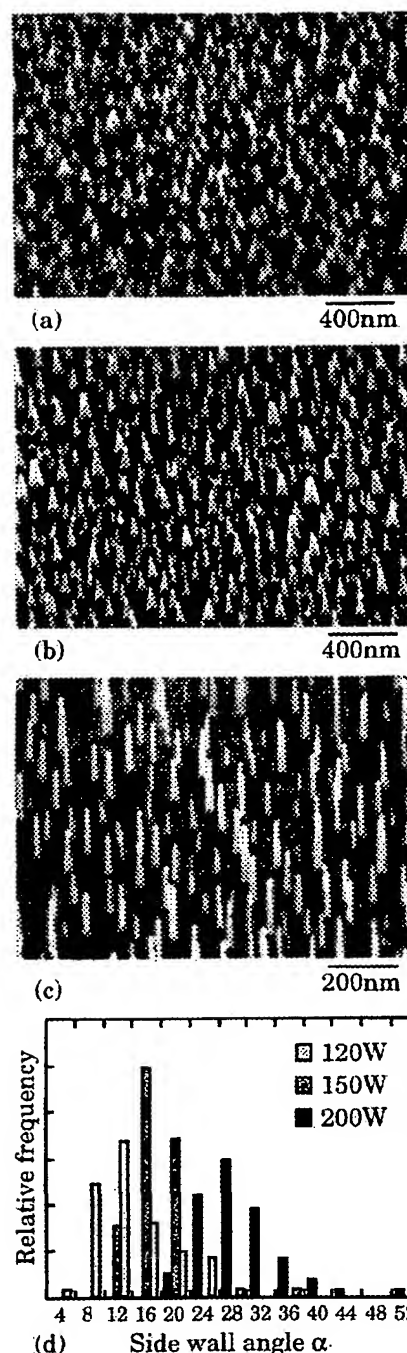


FIG. 3. Scanning electron micrographs (tilt angle 30°) of the silicon samples etched at different rf powers, (a) 200 W, (b) 150 W, (c) 100 W, and (d) distribution of apex angles of the cones for various etching powers above 100 W.

The influence of the etching time on samples etched at 100 W is shown in Fig. 4. The initial average thickness of the deposited silver film was 20 nm. After an etching time of 2 min, Fig. 4(a), the silicon pillars have a diameter of up to ~ 40 nm, which correlates with the diameter of the larger clusters shown in Fig. 1. Increasing the etching time to 2 min and 45 s, Fig. 4(b), results in a lower density of thinner pillars with typical diameters of < 10 –20 nm. We attribute this effect to slow sideways etching. Pillar diameters of less than 5 nm and an aspect ratio of height to diameter of up to

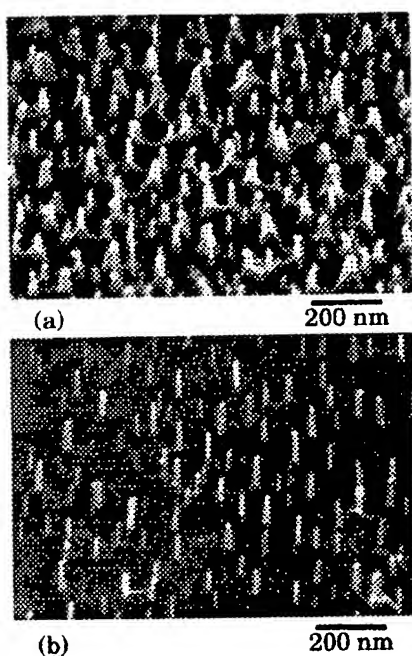


FIG. 4. Scanning electron micrographs (tilt angle 30°) of samples etched at 100 W for different times: (a) 2 min and (b) 2 min 45 s.

20:1 have been observed. Note also that the height of the pillars does not increase significantly with the etching time, which could also be due to some undercut of the silver masks.

Looking to the future, our results suggest that the width of distributions of the height and diameter of the pillars and cones, attributed to the irregular morphology of the silver film, could be reduced by the use of size-selected clusters. This would also allow control over the density of the structures. The deposition of size-selected clusters produced in a cluster beam source²² and the deposition of passivated clusters from solution²³ both represent attractive possibilities. The size and shape of the clusters should also influence the height of the resulting silicon structures. Since the sputter rate of the masks plays an important role in the shapes of the silicon features which are formed, it would also be interesting to investigate the use of different materials, such as gold or copper, as etching masks. This would be additionally beneficial because the initially chosen material, silver, is not complementary metal-oxide-semiconductor (C-MOS) compatible.

In summary, we have developed a simple but efficient method of producing nanoscale silicon cones and pillars over

wide areas, by utilizing rough silver films as etching masks. Reactive ion etching with a mixture of SF₆ and CF₄ gases gives anisotropic etching of the silicon. The variation of rf power allows us to control the shape of the resulting features (i.e., cone angle). Variation of the etching time allows us to control the diameter of the silicon pillars so that pillars as narrow as 5 nm can be produced.

This work was supported by the Engineering and Physical Sciences Research Council (EPSRC) and the European Regional Development Fund (ERDF). One of the authors (K.S.) would like to thank the University of Birmingham for the award of a studentship.

¹L. T. Canham, *Appl. Phys. Lett.* **57**, 1046 (1990).

²S. H. Zaidi, A. Chu, and S. R. J. Brueck, *J. Appl. Phys.* **12**, 6997 (1996).

³R. T. Tso, X. L. Li, and E. H. Nicollian, *Appl. Phys. Lett.* **65**, 842 (1994).

⁴A. G. Nassiopoulou, S. Grigoropoulos, and D. Papadimitrou, *Appl. Phys. Lett.* **69**, 2267 (1996).

⁵A. P. G. Robinson, R. E. Palmer, T. Tada, T. Kanayama, M. T. Allen, J. A. Preece, and K. D. M. Harris (unpublished).

⁶W. Chen and H. Ahmed, *Appl. Phys. Lett.* **63**, 1116 (1993).

⁷P. B. Fischer and S. Y. Chou, *Appl. Phys. Lett.* **62**, 1414 (1993).

⁸E. Gogolides, S. Grigoropoulos, and A. G. Nassiopoulou, *Microelectron. Eng.* **27**, 449 (1995).

⁹A. G. Nassiopoulou, S. Grigoropoulos, E. Gogolides, and D. Papadimitrou, *Appl. Phys. Lett.* **66**, 1114 (1995).

¹⁰T. Tada, T. Kanayama, K. Koga, K. Seeger, S. J. Carroll, P. Weibel, and R. E. Palmer, *Microelectron. Eng.* **41/42**, 539 (1998).

¹¹T. Tada, T. Kanayama, K. Koga, P. Weibel, S. J. Carroll, K. Seeger, and R. E. Palmer, *J. Phys. D* **31**, L21 (1998).

¹²G. W. Jones, C. T. Sune, and H. F. Gray, *IEEE Trans. Compon., Hybrids, Manuf. Technol.* **15**, 1051 (1992).

¹³E. I. Givargizov, V. V. Zhirnov, N. N. Chubun, and A. N. Stepanova, *J. Vac. Sci. Technol. B* **15**, 450 (1997).

¹⁴S. E. Huq, G. H. Grayer, S. W. Moon, and P. D. Prewett, *Mater. Sci. Eng., B* **51**, 150 (1998).

¹⁵H. S. Uh, S. J. Kwon, and J. D. Lee, *J. Vac. Sci. Technol. B* **15**, 472 (1997).

¹⁶J. H. Je, T. S. Kang, and D. Y. Noh, *J. Appl. Phys.* **10**, 6716 (1997).

¹⁷K. Tsujimoto, S. Okudaira, and S. Tachachi, *Jpn. J. Appl. Phys., Part 1* **30**, 3319 (1991).

¹⁸The mixture of gases was selected in the light of publications reporting on highly anisotropic etching using SF₆ and CHF₃ (see Ref. 19).

¹⁹S. Grigoropoulos, E. Gogolides, A. D. Tserpi, and A. G. Nassiopoulou, *J. Vac. Sci. Technol. B* **15**, 640 (1997).

²⁰An important practical detail is that for pillar formation the sample needs to be glued to the electrode with a small amount of vacuum grease. We believe that this is mainly to enhance the thermal contact to the water-cooled electrode, as reported by other authors. See, for example, Ref. 21.

²¹H. Jansen, H. Gardeniers, M. de Boer, M. Elwenspoek, and J. Fluitman, *J. Micromech. Microeng.* **6**, 14 (1996).

²²I. M. Goldby, B. v. Issendorff, L. Kuipers, and R. E. Palmer, *Rev. Sci. Instrum.* **68**, 3327 (1997).

²³J. P. Wilcoxon, R. L. Williamson, and R. Baughman, *J. Chem. Phys.* **98**, 9933 (1993).

Mechanisms of visible photoluminescence from nanoscale silicon cones

A. Wellner^{a)} and R. E. Palmer^{b)}

Nanoscale Physics Research Laboratory, School of Physics and Astronomy, The University of Birmingham, Edgbaston, Birmingham B15 2TT, United Kingdom

J. G. Zheng^{c)} and C. J. Kiely

Department of Engineering, Materials Science and Engineering, University of Liverpool, Liverpool, L69 3BX, United Kingdom

K. W. Kolasinski^{d)}

School of Chemistry, The University of Birmingham, Edgbaston, Birmingham B15 2TT, United Kingdom

(Received 24 July 2001; accepted for publication 12 December 2001)

We explore the origin of visible photoluminescence in nanoscale silicon cones fabricated by reactive ion etching in silicon-on-insulator substrates utilizing rough silver films as masks. Photoluminescence (PL) visible to the naked eye was observed after oxidation and annealing. Samples oxidized at 900 °C exhibit intense yellow/green photoluminescence centered at about 530 nm. Samples oxidized at 1000 °C luminesce in the red-to-infrared region with peak positions between 650 and 730 nm. Transmission electron microscopy characterization is employed to show that PL at 530 nm can be understood in terms of defect states, while the PL at 650–730 nm can be explained by a combination of defect state and quantum confinement effects. © 2002 American Institute of Physics. [DOI: 10.1063/1.1448394]

I. INTRODUCTION

The discovery of visible photoluminescence (PL) from porous silicon by Canham¹ has motivated extensive studies of silicon nanostructures.^{2,3} Despite intense investigation, the mechanism of light emission from silicon nanostructures is still not entirely understood. Canham¹ and many other workers^{2–6} have ascribed the photoluminescence to quantum confinement effects, supported by the observation that the luminescence shifts to shorter wavelengths with decreasing dimensions of the relevant silicon structures. However, silicon nanostructures are often oxidized and it has emerged in recent years that this oxidation of the nanoscale silicon structures also plays an important role in the photoluminescence mechanism. Depending on the size of the silicon nanostructures, silicon-oxide interface states can emerge in the band gap and act as recombination centers.^{7,8} Moreover, much of the continuing debate concerning photoluminescence from silicon nanostructures centers on the importance of luminescence from defects in the silicon oxide itself, which can overlap with photoluminescence bands from the nanoscale silicon structures.^{9–11} To resolve such questions in a convincing fashion, the coupling of optical measurements with high resolution measurements of the relevant structural elements is crucial.

Silicon nanostructures, including porous silicon,^{1–3,7,8} silicon clusters^{4,9,12,13} and silicon/silicon oxide quantum wells,^{5,6,14} can be produced by a variety of routes. Here we employ plasma etching with metal islands masks^{15–20} to produce nanoscale silicon cones. Such masks can also be defined by optical^{21–23} or electron beam^{24–27} lithography. However, only a few of these studies report luminescence^{19,23,24,26} and the observed wavelengths differ considerably. Building on the process developed by Seeger and Palmer,²⁰ which employs Ag island masks, we have successfully produced luminescent nanoscale silicon cones by reactive ion etching and have systematically investigated the mechanisms responsible for their photoluminescence. A key component in this work is the correlation between the optical properties observed and electron microscopy analysis of the silicon structures, which allows us to determine the mechanism of emission, e.g., to distinguish between the roles of quantum confinement and oxide states.

II. EXPERIMENT

The fabrication process for silicon pillars and cones has been discussed in detail in a previous article,²⁰ where it was shown that the etching time and applied rf power control the pillar shape and height. The silicon cones were etched in silicon-on-insulator (SOI) wafers using rough Ag films as etch masks. SOI wafers were employed to create a wide band gap layer below the fabricated Si nanostructures in order to enhance quantum confinement effects. The SOI (100) wafers featured a surface Si layer of thickness 200 nm separated from the bulk Si crystal by a 400 nm layer of SiO₂. In order to create a reference system, cones were also etched in Si(111) substrates (3° miscut, *p*-type, 8–12 Ω cm), which were processed under exactly the same conditions.

^{a)}Present address: Laboratoire de Physique des Solides de Toulouse UMR 5477, Université Paul Sabatier, 118 route de Narbonne, 31062 Toulouse cedex 4, France

^{b)}Author to whom correspondence should be addressed; electronic mail: r.e.palmer@bham.ac.uk

^{c)}Present address: Department of Materials and Engineering, Northwestern University, Evanston, IL 60208

^{d)}Present address: Department of Chemistry, Queen Mary, University of London, Mile End Road, London E1 4NS, United Kingdom

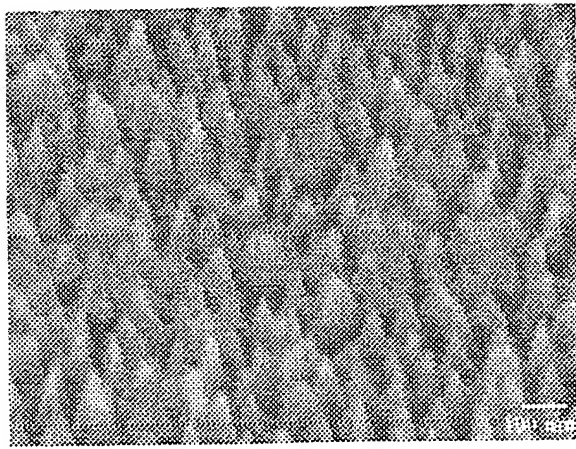


FIG. 1. Scanning electron micrograph (specimen tilt angle 30°) of silicon cones fabricated by reactive ion etching of a silicon-on-oxide wafer (after cleaning).

A magnetron sputter coater (Edwards Auto 306) was used to deposit a 5 nm Ag film at an Ar pressure of 7×10^{-2} mbar and a rf power of 25 W, which corresponds to a flux rate of about 1 nm min^{-1} . The samples were etched in a commercial reactive ion etching (RIE) machine (Oxford Plasmalab 80+,) for 95 to 110 s with an applied rf power of 100 W, resulting in a self-bias at the sample electrode of between -417 and -423 V. The etchant gas used was a mixture of SF_6 and CF_4 introduced at a flow rate ratio of 25 sccm:25 sccm and a pressure of 6 mTorr.

In order to remove the remains of the Ag mask after etching, the cones were cleaned by immersing the samples in a 4:1 solution of $\text{H}_2\text{SO}_4:\text{H}_2\text{O}_2$ for 10 min at room temperature. They were rinsed in deionized water, then ethanol and dipped into HF to remove the native oxide layer. This process was followed by another sequential rinse in deionized water and ethanol. The samples were then blow dried. Figure 1 is a scanning electron micrograph of the cones after the cleaning procedure. The diameter of the cones lies in the range 30 to 100 nm at the base and their height varies between 130–180 nm.

The samples produced were oxidized in a dry oxygen atmosphere (Carbolite tube furnace) at 900°C or 1000°C for different durations followed by annealing for the same length of time in dry nitrogen at the same temperature. The PL measurements were taken in air at room temperature between oxidation steps, and employed a frequency doubled Argon ion laser which provides an excitation wavelength of 244 nm. The emitted light was collected with an $f=50$ mm camera lens and focussed onto the entrance slit of a 0.25 m spectrometer (Jobin Yvon). The spectrometer consists of a TRIAX 190 single grating monochromator and a SPEX iCCD detector operated at a temperature of 250 K.

Samples for transmission electron microscopy were prepared by cleaving a thin slice off the wafer and mounting it on a copper support ring, such that the original (001) Si surface was close to perpendicular to the ring. The resulting wedge is sufficiently thin to allow electron transmission imaging of cones. This sample preparation method ensures

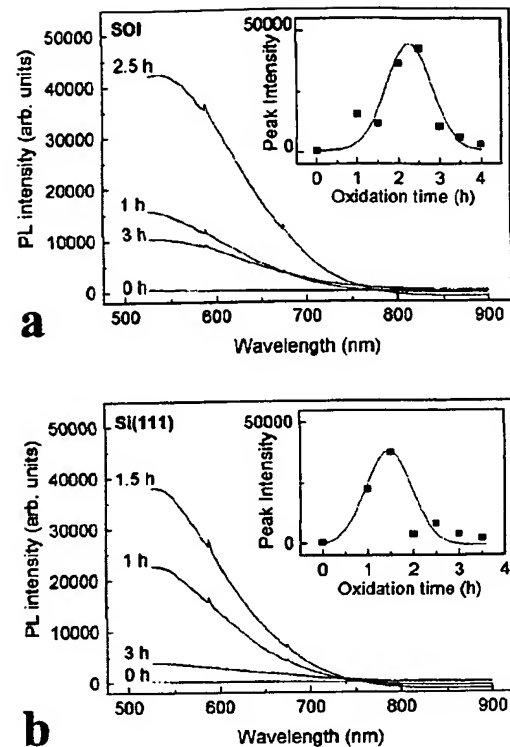


FIG. 2. Typical PL spectra of silicon cones oxidized at 900°C , etched in (a) silicon-on-insulator (SOI) and (b) Si(111) substrates. The insets show the evolution of the peak intensities with oxidation time; the lines are drawn to guide the eye.

minimal mechanical damage of the cones. The samples were examined in a VG HB601UX scanning transmission electron microscope (STEM) operating at 100 kV and equipped with a GATAN 666 parallel electron energy loss spectrometer (PEELS). A JEOL 200 CX TEM operating at 200 kV was employed for conventional bright field and dark field imaging.

III. RESULTS

A. Silicon cones oxidized at 900°C

Figure 2(a) shows typical PL spectra of silicon cones in SOI after oxidation at 900°C . The samples show no photoluminescence immediately after etching and cleaning but after oxidation for 1 h a broad PL signal centered at about 510–530 nm appears. This PL signal continues to grow in intensity with repeated oxidation until it reaches a maximum after 2.5 h, and then decreases until it has almost completely disappeared after 4 h of oxidation. The inset shows the evolution of the peak intensity (the line is drawn to guide the eye). Silicon cones etched in a Si(111) substrate to act as control samples show very similar behavior, Fig. 2(b). It should be noted that the PL intensity for both substrates can vary significantly across the sample, very likely due to inhomogeneities in the masking and etching process. Therefore, an effort was made to relocate and measure, as far as possible, the same spot on the sample after each oxidation step.

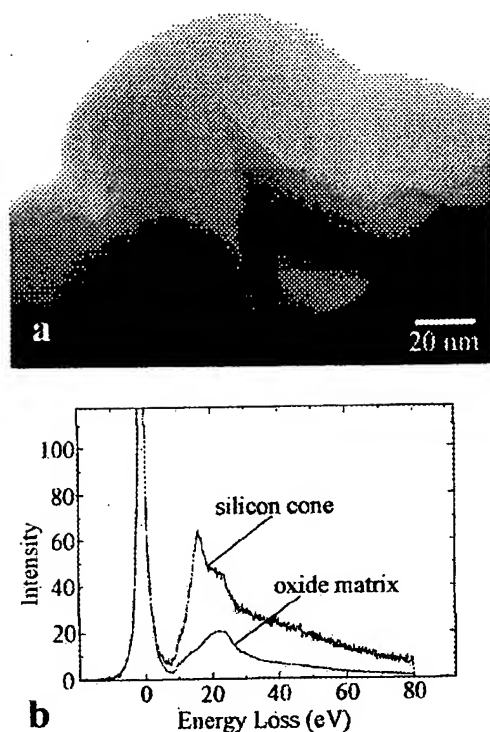


FIG. 3. (a) STEM bright field micrograph of a silicon cone embedded in silicon oxide, produced by RIE of a SOI substrate and subsequent oxidation for 30 min at 900 °C; (b) electron energy loss spectra taken from the tip of the cone and the surrounding oxide matrix.

The evolution of the intensity has been observed for several different positions on a given sample as well as for different samples.

The structure of the silicon cones was investigated by STEM. Figure 3(a) is a bright field STEM micrograph of a sample, etched in an SOI substrate and oxidized for 30 min at 900 °C, which exhibited intense yellow photoluminescence. The figure shows strong diffraction contrast from a silicon cone embedded in a silicon oxide mound having a wall thickness of 35 to 40 nm. The tip of the cone is very sharp, with a diameter below 5 nm. Electron energy loss spectra (EELS) of the cone acquired with a 1 nm probe confirm that it still contains silicon in its interior. Figure 3(b) shows spectra taken just below the tip of the strongly diffracting cone and from the less contrasty surrounding oxide matrix. The spectrum taken just below the tip of the cone clearly shows the Si bulk plasmon peak at 17 eV; the shoulder in this spectrum arises from the overlying silicon oxide plasmon peak at 24 eV, as can be seen by comparison with the spectrum taken only from the silicon oxide skin.

B. Silicon cones oxidized at 1000 °C

Samples oxidized and annealed at 1000 °C show very different behavior. Figure 4(a) shows typical PL spectra of silicon cones etched in SOI. The samples show no PL, either directly after etching, or after 1 h of oxidation. However, after 2 h of oxidation, photoluminescence visible to the eye appears in the red region. The peak position is correlated

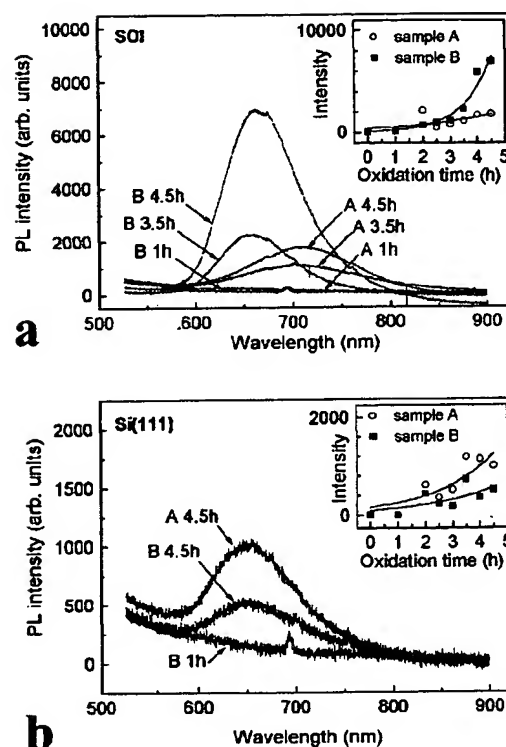


FIG. 4. Typical PL spectra of silicon cones oxidized at 1000 °C, etched in (a) SOI and (b) Si(111) substrates. The insets show the evolution of the peak intensities with oxidation time; the lines are drawn to guide the eye.

with the RIE etching time in the cone fabrication process. Sample A, etched for 95 s, displays a peak centered at about 730 nm (1.7 eV), which does not shift with repeated oxidation, while sample B, etched for 110 s, displays a peak centered at about 650 nm, which shifts to 670 nm with successive oxidations. The peak intensity increases with repeated oxidation [inset to Fig. 4(a), where the lines are drawn to guide the eye] but is between 5 and 20 times less intense than the maximum photoluminescence intensity observed from samples oxidized at 900 °C. Control samples etched on Si(111) also exhibit red PL, Fig. 4(b), but the photoluminescence is very weak (i.e., much weaker than from the SOI samples). After 2 h of oxidation and annealing a peak centered at about 650 to 670 nm appears; the peak position shows no correlation with the cone etching time. The photoluminescence intensity increases slightly with continued oxidation [inset to Fig. 4(b)] and in the spectra taken after 4.5 h of oxidation a peak is clearly evident in the spectrum.

The structure of the silicon cones oxidized at 1000 °C was investigated by conventional TEM. Figure 5 shows representative TEM micrographs of cones etched in an SOI substrate and oxidized for 2 h at 1000 °C. The sample showed red photoluminescence centered at 730 nm [sample A in Fig. 4(a)]. Figure 5(a), an axial [111] bright field image, shows that the tops of the cones are amorphous due to complete oxidation. However, at the base of the cones, close to the buried oxide, a crystalline region is visible. In Fig. 5(b), an axial [111] dark field image of the area taken with the (220) diffraction spot, clearly shows diffraction contrast from a

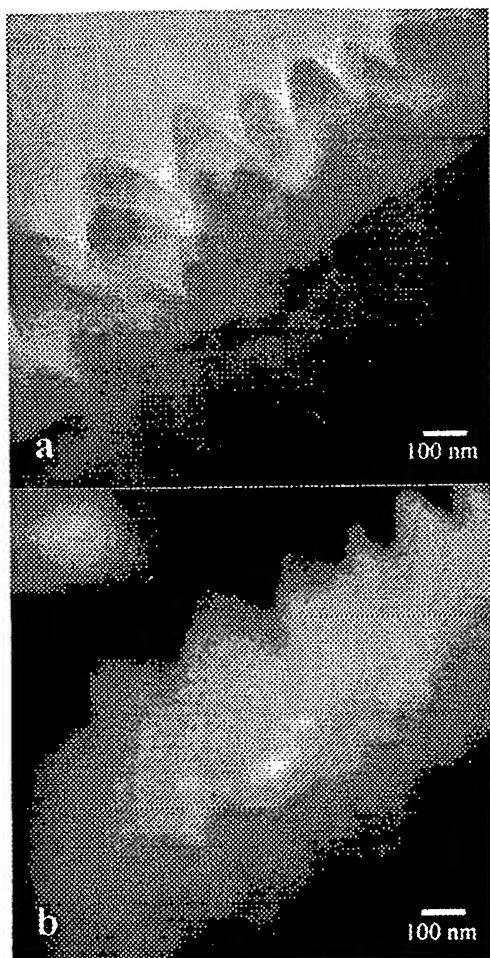


FIG. 5. Transmission electron micrograph of silicon cones etched in an SOI substrate and oxidized for 2 h at 1000 °C. (a) Axial [111] bright field image; (b) axial [111] dark field image taken with the (220) diffraction spot and (inset) selected area diffraction pattern.

crystalline silicon cluster at the interface. The selected area diffraction pattern of the cluster [inset to Fig. 5(b)] shows that it consists of crystalline silicon close to the [111] orientation. Such silicon clusters could still be found in sample A after 4.5 h of oxidation. By contrast, sample B (having a longer cone etching time), which showed photoluminescence centered around 650 to 670 nm, did not contain any crystalline silicon. The cones were totally amorphous and fully oxidized throughout, even after only 2 h of oxidation.

IV. DISCUSSION

A. Photoluminescence of silicon cones oxidized at 900 °C

Photoluminescence in the blue to yellow region has been commonly reported for silicon/silicon oxide systems. For example, Mutti *et al.*¹² observed PL at 490–540 nm from Si⁺ implanted SiO₂ layers and ascribed it to quantum confinement in silicon nanocrystals. We do not believe that the yellow/blue PL from our cones is caused by a quantum confinement effect, since the Si cones are still far too large, as

can be seen from the STEM image (Fig. 3). Although the existence of a proportion of much smaller cones cannot be ruled out, a quantum confinement model is also inconsistent with the following observations: (i) cones etched on Si(111) (which are not electrically isolated from the bulk silicon) luminesce with similar intensity and wavelength to the cones on the insulating oxide layer, (ii) the peaks do not shift with increased oxidation, and (iii) the PL disappears following longer oxidation times. We believe (and other authors have argued similarly^{9,10,28}) that the blue/yellow photoluminescence originates from defect states. Nishikawa *et al.*¹⁰ reported PL bands at 400–517 nm from the buried oxide in SOI samples and ascribed them to interface states between the Si and the oxide. Song and Bao⁹ reported three bands centered at 470, 550, and 630 nm from Si⁺ implanted SiO₂ layers and showed that the intensities decreased with increasing annealing temperature and annealing time. They concluded that the PL arises from defects in the silicon oxide, such as neutral oxygen vacancies and nonbridging oxygen hole centers, and that the observed decrease in PL intensities is due to defect annealing. Defect creation and annealing is also the most likely explanation for the evolution of the PL intensity from our samples. The intensity increases during initial oxidation because more defects are created than are annealed out. Subsequently the oxidation rate decreases due to the self-limiting effect in small silicon structures for temperatures below 950 °C,^{27,29} and the interface advances progressively more slowly. In this regime, more defects are annealed out than are induced by oxidation and the PL intensity decreases, in harmony with the experimental results.

B. Photoluminescence of silicon cones oxidized at 1000 °C

Many authors^{1–6,9,12–14} have reported red to infrared photoluminescence for silicon/silicon oxide systems and most associated it with quantum confinement in silicon nanocrystals or thin silicon layers. However, red photoluminescence at 653 and 689 nm has been also observed from irradiated silica¹¹ and explained by PL from defect states, such as nonbridging oxygen hole centers and oxygen deficient states, respectively. We believe that the red PL observed from our samples arises from both defect states and quantum confinement. The existence of weak PL at about 650 to 670 nm from silicon cones etched on a Si(111) substrate suggests that photoluminescence at these wavelengths arises from defects in the grown oxide, since the cones are not electrically isolated from the substrate. This is supported by the fact that cones etched in SOI which showed photoluminescence at these same wavelengths were oxidized throughout and did not contain any crystalline silicon. The higher photoluminescence intensity from cones etched in SOI then most likely arises from a contribution due to the buried oxide.

By way of contrast, cones etched on top of the buried oxide layer in the SOI substrates, which showed photoluminescence at longer wavelengths (730 nm) contained crystalline silicon clusters at their base. This suggests that this band of red photoluminescence is caused by a quantum confinement effect in these silicon clusters. When invoking a quantum confinement effect, we include the scheme in which con-

finement increases the band gap and exposes the localized states at the Si/SiO₂ interface, which may then dominate the recombination process, as has been discussed previously for porous silicon^{7,8} and Si/SiO₂ quantum wells.¹⁴

V. CONCLUSION


Silicon nanocones have been fabricated in silicon-on-insulator and Si(111) substrates by reactive ion etching utilizing rough silver films as masks. The samples exhibited visible photoluminescence after repeated oxidation in a dry oxygen atmosphere and annealing in nitrogen. Samples oxidized at 900 °C were found to emit yellow/green light with intensities, which were similar for the two substrates. It was shown that this photoluminescence band and the evolution of its intensity with oxidation time can be understood in terms of the creation and annealing-out of defects. By contrast, samples oxidized at 1000 °C exhibit red photoluminescence. The photoluminescence is centered at 650 to 670 nm for cones etched in Si(111) substrates and 650 to 730 nm for cones etched in silicon-on-insulator substrates. It was shown that photoluminescence centered at 650 to 670 nm most likely arises from defect states in the oxide, whereas the photoluminescence from the SOI cones centered at longer wavelengths can be attributed to a combination of a quantum confinement effects in silicon clusters together with the contribution of Si/SiO₂ interface states.

The results demonstrate, to the best of our knowledge, the first silicon nanocones fabricated by reactive ion etching in silicon-on-insulators which exhibit photoluminescence. In the future it would be interesting to explore the photoluminescence properties of ordered arrays of silicon cones or pillars^{30,31} in view of their narrower size distribution and because such structures may also display a photonic band gap.

ACKNOWLEDGMENTS

The authors thank the EPSRC for support of this work. A.W. is grateful to Dr. R.N. Neuendorf for help with the photoluminescence measurements, to Dr. L. Koker and Dr. M. Bale for assistance in the sample preparations, and to Dr. G. R. Millward for help with the 200 CX TEM. The frequency doubled argon ion laser used in the PL measurements was provided by the EPSRC Laser Loan Pool.

- ¹L. T. Canham, *Appl. Phys. Lett.* **57**, 1046 (1990).
- ²A. G. Cullis, L. T. Canham, and P. D. J. Calcott, *J. Appl. Phys.* **82**, 909 (1997).
- ³B. Hamilton, *Semicond. Sci. Technol.* **10**, 1187 (1995).
- ⁴G. Ledoux, O. Guillois, D. Porterat, C. Reynaud, F. Huisken, B. Kohn, and V. Paillard, *Phys. Rev. B* **62**, 15 942 (2000).
- ⁵D. J. Lockwood, Z. H. Lu, and J. M. Baribeau, *Phys. Rev. Lett.* **76**, 539 (1996).
- ⁶P. Photopoulos, A. G. Nassiopoulou, D. N. Kouvatsos, and A. Ravlos, *Appl. Phys. Lett.* **76**, 3588 (2000).
- ⁷M. V. Wolkin, J. Jorne, P. M. Fauchet, G. Allan, and C. Delerue, *Phys. Rev. Lett.* **82**, 197 (1999).
- ⁸K. W. Kolasinski, J. C. Barnard, S. Ganguly, L. Koker, A. Wellner, M. Aindow, R. E. Palmer, C. N. Field, P. A. Hamley, and M. Poliakoff, *J. Appl. Phys.* **88**, 2472 (2000).
- ⁹H. Z. Song and X. M. Bao, *Phys. Rev. B* **55**, 6988 (1997).
- ¹⁰H. Nishikawa, R. E. Stahlbush, and J. H. Stathis, *Phys. Rev. B* **60**, 15 910 (1999).
- ¹¹Y. Sakurai, N. Nagasawa, H. Nishikawa, and Y. Ohki, *J. Appl. Phys.* **86**, 370 (1999).
- ¹²P. Mutti, G. Ghisloti, S. Bertoni, L. Bonoldi, G. F. Cerofolini, L. Meda, E. Grilli, and M. Guzzi, *Appl. Phys. Lett.* **66**, 851 (1994).
- ¹³T. Shimizu-Iwayama, D. E. Hole, and I. W. Boyd, *J. Phys.: Condens. Matter* **11**, 6595 (1999).
- ¹⁴Y. Kanemitsu and S. Okamoto, *Phys. Rev. B* **56**, R15 561 (1997).
- ¹⁵M. Gotza, M. Dutoit, and M. Illegems, *J. Vac. Sci. Technol. B* **16**, 582 (1998).
- ¹⁶T. Tada, T. Kanayama, K. Koga, K. Seeger, S. J. Carroll, P. Weibel, and R. E. Palmer, *Microelectron. Eng.* **41/42**, 539 (1998).
- ¹⁷T. Tada, T. Kanayama, K. Koga, P. Weibel, S. J. Carroll, K. Seeger, and R. E. Palmer, *J. Phys. D* **31**, L21 (1998).
- ¹⁸P. A. Lewis, H. Ahmed, and T. Sato, *J. Vac. Sci. Technol. B* **16**, 2938 (1998).
- ¹⁹A. Malinin, V. Ovchinnikov, S. Novikov, C. Tuovinen, and A. Hovinen, *Mater. Sci. Eng., B* **74**, 32 (2000).
- ²⁰K. Seeger and R. E. Palmer, *Appl. Phys. Lett.* **74**, 1627 (1999).
- ²¹S. H. Zaidi, A. Chu, and S. R. J. Brueck, *J. Appl. Phys.* **80**, 6997 (1996).
- ²²A. G. Nassiopoulou, S. Grigoropoulos, and D. Papadimitriou, *Appl. Phys. Lett.* **69**, 2267 (1996).
- ²³A. G. Nassiopoulou, S. Grigoropoulos, E. Gogolides, and D. Papadimitriou, *Appl. Phys. Lett.* **66**, 1114 (1995).
- ²⁴P. B. Fischer and S. Y. Chou, *Appl. Phys. Lett.* **62**, 1414 (1993).
- ²⁵W. Chen and H. Ahmed, *Appl. Phys. Lett.* **63**, 1116 (1993).
- ²⁶P. B. Fischer, K. Dai, E. Chen, and S. Y. Chou, *J. Vac. Sci. Technol. B* **11**, 2524 (1993).
- ²⁷H. Heidemeyer, C. Single, F. Zhou, F. E. Prins, D. P. Kern, and E. Plies, *J. Appl. Phys.* **87**, 4580 (2000).
- ²⁸D. P. Yu, Z. G. Bai, J. J. Wang, Y. H. Zhou, W. Qian, J. S. Fu, H. Z. Zhang, Y. Ding, G. C. Xiong, L. P. You, J. Xu, and S. Q. Feng, *Phys. Rev. B* **59**, R2498 (1999).
- ²⁹H. I. Lui, D. K. Biegelsen, F. A. Ponce, N. M. Johnson, and R. F. W. Pease, *Appl. Phys. Lett.* **64**, 1383 (1994).
- ³⁰K. Seeger and R. E. Palmer, *J. Phys. D* **32**, L129 (1999).
- ³¹A. Wellner, P. R. Preece, J. C. Fowler, and R. E. Palmer, *Microelectron. Eng.* **57-58**, 919 (2001).

A.J. PEDRAZA 
J.D. FOWLKES
Y.-F. GUAN

Surface nanostructuring of silicon

Department of Materials Science and Engineering, The University of Tennessee,
Knoxville, TN 37996-2200, USA

Received: 16 December 2002 / Accepted: 20 January 2003
Published online: 28 May 2003 • © Springer-Verlag 2003

ABSTRACT Irradiation with polarized laser light of 248-nm wavelength induces the formation of periodic undulations ~ 10 -nm-high on flat silicon substrates. The wavelength of these periodic structures is a function of the light wavelength and the angle of incidence of the laser beam. Linear arrays of silicon nanoparticles with fairly uniform size that extended up to a millimeter were formed if the irradiation was performed using polarized light. When non-polarized laser light with the same fluence was used to illuminate an initially flat surface, non-aligned nanoparticle strings were obtained. However, if part of the irradiated area was microstructured, nanoparticle linear arrays resulted in the vicinity of the microstructured region. An analysis on the evolution of these nanostructures is presented. Nanocolumns could be grown on top of every cone of a microstructured surface upon cumulative laser irradiation with non-polarized light, reaching a height of $\sim 3 \mu\text{m}$ and a diameter of 100–200 nm. The mechanisms of nanocolumn origin and growth are analyzed.

PACS 61.46.+w; 61.80.Ba; 61.82.Fk; 68.35.Bs

1 Introduction

Laser-induced surface microstructuring of silicon has been extensively studied [1–8], and has been found to be a function of fluence and of the composition and pressure of the background atmosphere present in the irradiation chamber [5, 6]. At a fluence between 2 and 3 J/cm^2 two distinct processes can take place sequentially as a result of cumulative laser irradiation. Shallow depressions evolve and can reach a depth of a few micrometers and a separation distance of 20 to $30 \mu\text{m}$ [7]. These depressions are initially sparsely distributed on the surface, but new ones form and progressively cover the entire irradiated area. At the same time, the depressions continuously deepen with the number of laser pulses. For irradiation in non-reactive environments such as vacuum or Ar, this surface relief continuously builds up with the number of laser pulses, up to 10 000 pulses [8].


In a reactive atmosphere like SF_6 , the same evolution is initially observed in the same fluence range, but more dramatic changes occur after 600 pulses. Additional irradiation in

SF_6 produces a drastic change both in the surface-roughening rate and in the morphology, establishing the signature of a second, different process. The change to this second process, which produces a characteristic microhole–microcone microstructure, is preceded by a transition stage in the morphology. Figure 1 shows the three stages of microstructure evolution just outlined. After ~ 400 laser pulses, the surface relief depends only on the crystallographic orientation of the laser-exposed surface. The optical image acquired with Nomarski contrast shown in Fig. 1a illustrates the first stage in the process of a surface relief production. Shallow depressions and elevations that have the appearance of a cube structure can be seen. The orientation of the surface is very close to (111) and the characteristic three-fold symmetry is clearly revealed by the surface traces. The same relief is produced under reactive and non-reactive atmospheres. The second stage, shown in Fig. 1b, has been observed only under a reactive (SF_6) irradiation atmosphere and after a higher number of pulses. Intense etching takes place at the bottom of the depressions formed during stage 1. Multiple reflections focus the beam at these depressions, enhancing the decomposition of SF_6 and thus the etching activity [8]. The third stage (Fig. 1c) is characterized by a synergistic process involving hole deepening by etching-assisted ablation and cone growth by re-deposition of ablated species on top and to the sides of the laser-melted regions. Since ablation also takes place in these regions, growth can occur only when re-deposition occurs in excess of ablation.

A reduction of the laser energy to $\leq 1 \text{ J/cm}^2$ drastically changes the scale of the surface relief, promoting the formation of nanostructures. Three different phenomena will be described and analyzed: (1) the production of periodic nanochannels; (2) the formation of an organized array of nanoparticles; and (3) the growth of nanocolumns. The processing characteristics could be of interest for some technologies, since long-range ordering of nanostructures is a key issue, central to the utilization of nanostructures in electronic materials applications.

2 Experimental procedure

Boron-doped silicon substrates were irradiated using a Lambda Physik LPX-305i KrF excimer laser (248-nm wavelength), with a pulse duration of 25 ns. Unless otherwise

 Fax: +1-865/974-4115, E-mail: apedraza@utk.edu

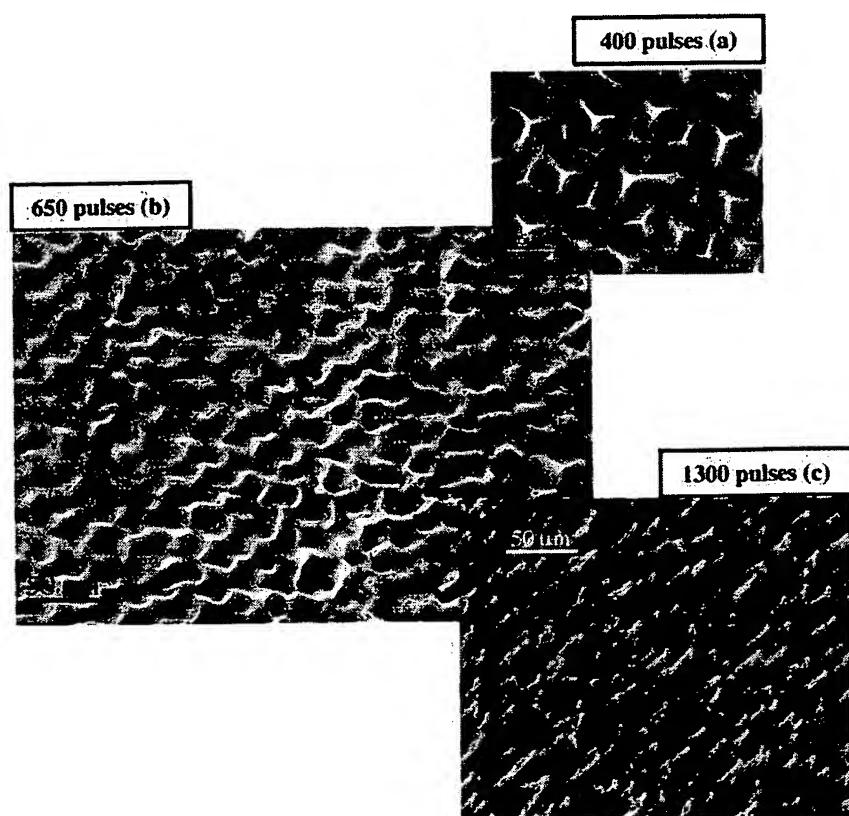


FIGURE 1 The three stages of cone formation in silicon under an SF_6 atmosphere. **a** Optical micrograph with Nomarski contrast; **b** and **c** SEM images with sample tilted 40°

indicated, all laser treatments were carried out at normal incidence. The beam emerging from the laser cavity was directed to an optic bench using a MgF_2 -coated fused-silica mirror. The optic bench contained an aperture, a fused-silica lens array, and the irradiation chamber. The rectangular aperture partly removed the low energy tails of the trapezoidal laser beam. The laser fluence was varied by adjusting the position of the fused-silica lens array relative to the sample holder in the irradiation chamber.

All of the experiments were conducted using helium as background gas. For each laser irradiation cycle, the irradiation chamber was pumped to a base pressure of 1×10^{-7} Torr

He prior to introducing 99.999% pure helium gas at a selected pressure. For some experiments, the substrates were first laser-microstructured in an SF_6 atmosphere, to produce a cone relief.

Native oxide layer removal was done by immersing the specimens in a 10 : 1 HF aqueous solution for 5 min, washing, drying and quickly transferring them to a vacuum chamber. Table 1 summarizes the experimental conditions used for the examples shown in the figures.

Ex situ characterization studies were conducted using scanning electron microscopy (SEM), atomic force microscopy (AFM), and Auger emission spectroscopy (AES).

Figure number	Laser fluence (J/cm^2) and polarization (p,np) ^a	Number of pulses	Composition and pressure (Torr) of irradiation atmosphere	Initial surface topography	Final surface structure
2	0.8 p	400	Vacuum 1×10^{-6}	Smooth ^b	Nanochannels
3	0.6 np	450	He 100	Smooth ^c	Nanoparticles
4a	0.6 np	500	He 100	Smooth ^c	Nanoparticles
4b	0.6 np	700	He 100	Smooth ^c	Nanoparticles
5	1 np	200	He 100	Smooth ^c + Cones	Nanoparticle clusters and ordered nanoparticle array
6	1 np	200	He 0.5	Smooth ^c + Cones	Ordered nanoparticle array
7	0.5 np	2000	He 10	Microcones	Nanocolumn (Start)
8	0.5 np	0–10 000	He 10	Microcones	Nanocolumn on top of cone
9	0.5 np	15 000	He 10	Microcones	Nanocolumn on top of cone

^a p: polarized; np: non-polarized

^b native oxide present in surface

^c native oxide removed

TABLE 1 Summary of experimental conditions related to figures

3 Formation of nanochannels by laser irradiation

The formation of nanochannels was observed only when using polarized light to irradiate silicon specimens and when the surface had its native oxide. In order to examine the effect of the presence of this oxide layer, two types of experiment were first performed, using the same conditions: 2000 pulses of polarized laser light at an angle of incidence of 14° , a fluence of 0.7 J/cm^2 and a vacuum pressure of 5×10^{-6} Torr. In one of the experiment types, the native oxide was removed from the surface of the silicon targets prior to the irradiation, while for the other type, specimens with the native oxide were irradiated without any surface conditioning. These experiments consistently showed that the oxide layer stabilizes the ripples. All the experiments described in this section were performed on silicon with the native oxide film using polarized light.

Formation of 6–10-nm-deep nanochannels was induced by laser irradiation of an initially flat silicon substrate, in a background pressure of 1×10^{-6} Torr, at a laser fluence of 0.8 J/cm^2 . These channels were produced using linearly p-polarized light (for which the electric field lies in the plane of incidence) and were aligned normal to the polarization direction. At normal laser beam incidence, the spacing between channels, Λ , equaled the laser wavelength, λ . The channels were not featureless, as can be seen in Fig. 2. The overall structure could be described as two periodic structures or waves of the same wavelength displaced from each other by half a wavelength. The amplitude of one of the waves was

$\sim 6 \text{ nm}$ – significantly larger than the amplitude of the other wave.

Several experiments were done with an angle of incidence of the beam $\theta > 0$. In this case, two line-spacings were found in the same specimen in some instances. For example, for a sample irradiated with 2000 pulses at a fluence of 1 J/cm^2 in a 10 Torr background pressure of He and for $\theta = 15^\circ$, the two spacings given in the first column of Table 2 were measured.

The spontaneous formation of periodic ripples on the surface of a material illuminated with polarized pulsed laser light has been reported in many different materials [9–23] at fluences close to the melting threshold, spanning a wavelength range of 10.6 to $0.193 \mu\text{m}$. The period and orientation of these surface ripples, known in the literature as laser-induced periodic surface structures (LIPSS), mainly depend on the following aspects of the laser beam: angle of incidence, polarization, frequency, and energy. However, the occurrence of LIPSS in a given material appears to be a strong function of the specific response of this material to inhomogeneous energy deposition. For instance, for a given set of the main laser parameters just listed, some fringe patterns observed in Ge have not been detected in Si or Al [12]. Excluding the studies in polymers, all of the previous reports refer to LIPSS spacings on the order of microns. This is the first time that nano-LIPSS have been demonstrated in silicon.

The most often encountered periodic structures are those whose wave vector is parallel to the projection of the electric field on the surface plane [12]. These ripples or fringes were found mostly when the electromagnetic field was linearly polarized, whether the electric field lay in the plane of incidence (p-polarized) or perpendicular to it (s-polarized). LIPSS could be very simply interpreted as being produced by the interference between the refracted radiation and two scattered waves parallel to the surface propagating in opposite directions, giving the following dependence of fringe spacings, Λ_+ and Λ_- , on the angle of incidence θ and the laser wavelength λ :

$$\Lambda_{\pm} = \frac{\lambda}{1 \pm \sin \theta} \quad (1)$$

As can be seen from Table 2, the line-spacings calculated using (1) for the case of $\theta = 15^\circ$ and $\lambda = 248 \text{ nm}$ are in good agreement with the two values reported above of 204 nm and 331 nm. In addition, in some cases a spacing following a different law,

$$\Lambda = \frac{\lambda}{\cos \theta} \quad (2)$$

was found for fringes running parallel to the polarization vector of incident p-polarized light, in contrast with those whose spacing was described by the sine law, which run perpendicular to it [14, 15].

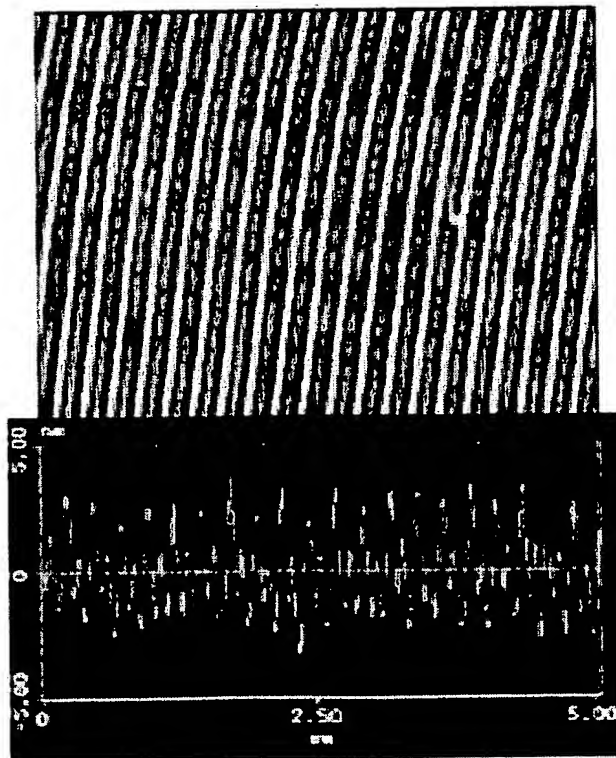


FIGURE 2 AFM image of LIPSS formed in silicon under vacuum. Linearly polarized laser light at normal incidence. Laser wavelength: 248 nm; fluence: 0.8 J/cm^2 ; 400 pulses. Note: y-scale in nm; x-scale in μm

$\Lambda_{\text{measured}} \text{ (nm)}$	$\Lambda = \frac{\lambda}{1 + \sin \theta}$	$\Lambda = \frac{\lambda}{1 - \sin \theta}$
204	197	–
335	–	331

TABLE 2 Measured and calculated line-spacing of LIPSS

Several groups have developed theories to explain the production of LIPSS [11, 13, 14, 23]. The key factor to explain LIPSS evolution in all of the models is the occurrence of an inhomogeneous light intensity distribution on the surface. The inhomogeneity in the light distribution arises from the interaction between the light scattered by surface roughness and the refracted laser light. There are several ways whereby the material can respond to the temperature modulation due to this energy inhomogeneity [13, 14]. It has also been recognized that a positive feedback is necessary for the ripples to be produced. Concurrent with this concept, we have observed in our studies that nanoripple formation always requires multiple laser pulses, also indicating that the interaction between roughness and light evolves with an increasing number of pulses. The difficulty in stabilizing this nanostructure is highlighted by two factors, possibly interrelated: the large number of pulses needed to form them, as just emphasized, and the apparent requirement that there must be a native oxide layer present.

4 Self-organized linear arrays of laser-induced silicon nanoparticles

All the experiments in this section, with one exception, were performed using non-polarized light. The native oxide was removed in all the specimens, flat and microstructured, prior to laser irradiation to minimize oxide contamination of the nanoparticles. At laser fluences close to 1 J/cm^2 and using a background atmosphere of ultra high purity (UHP) He rather than vacuum, a film was deposited on the surface of a silicon substrate [24]. The background gas backscattered atoms and probably very small clusters were also deposited on the substrate. The film detected by AFM using a tapping mode scan, after 200 pulses at 1 J/cm^2 and 10 Torr of He background pressure, was very porous with some areas a few nanometers thick and other areas with a much thinner film or no film at all. The average film thickness observed over all the measured specimens was of the order of 1 nm. However the film thickness did not increase very significantly after the first 50 pulses, giving an average deposition rate of $\sim 2 \times 10^{-2} \text{ nm/pulse}$. From this deposition rate, it is difficult to evaluate the average ablation rate during irradiation because in some regions of the specimen ablation was taking place, while in others there was material accumulation.

It is clear from the extensive work done on ripple formation that a non-uniform deposition of energy is produced during laser irradiation of a surface with micro- or nano-roughness. In our case, AFM images recorded very significant nano-roughness in all specimens, with some regions as high as 8 nm. Light scattering from this random nano-roughness will produce a random interference pattern with the refracted light that will generate a non-uniform energy deposition. For this reason, it is difficult to establish a meaningful correlation between the ablation rate and laser fluence. The fact that a film was formed at the same time as ablation was taking place indicates that the laser fluence used in these experiments was very close to the ablation threshold. The film did not seem to increase significantly with the number of pulses, probably due to continuous ablation and clustering. Auger emission spectroscopy revealed that beyond the first nanometer the film

was at least 90% silicon, with no silicon bound to an oxide or carbide.

SEM and AFM images indicate that the film clusters and forms nanoparticles as it is being irradiated with non-polarized laser light [24]. We have observed film-denuded zones, 1 to $2 \mu\text{m}$ in diameter, containing nanoparticles that had apparently consumed the film originally in the zone. The distance between nanoparticles in these small regions was close to the wavelength of the incident light, indicating a process controlled by a non-homogeneous distribution of energy similar to what happens during ripple formation.

As nanoparticle formation proceeded with additional irradiation, the particles tended to aggregate into curvilinear strings and became stabilized at $\sim 30 \text{ nm}$ -diameter, as measured in SEM images (Fig. 3). This behavior resulted in a fairly uniform size distribution. The evolution of this nanostructure with additional irradiation was followed using a high-precision SEM stage positioning mechanism. The nanoparticles kept their identity and shape; however, they experienced displacements, as illustrated in Fig. 4. They tended to align in short curvilinear strings like pearls in a necklace, and some ordering can be appreciated in the micrographs. At a certain point the strings became locked and further movement or ordering did not occur. At higher laser fluence, e.g., 1.3 J/cm^2 , they flattened and tended to fuse with the substrate.

A very dramatic change in the nanoparticle spatial distribution occurred when the irradiation was done on a surface partly covered with a well-developed cone microstructure. The microcones were grown by laser irradiation in a 0.5 bar SF_6 atmosphere, using 1200–2000 pulses at a laser energy of $\sim 3 \text{ J/cm}^2$; they had a height of 20–30 μm and tips of a few micrometers in diameter [6–8]. A typical microstructure is shown in Fig. 1c.

The irradiation in He resulted in film deposition and the formation of linear arrays in the regions of the irradiated sub-

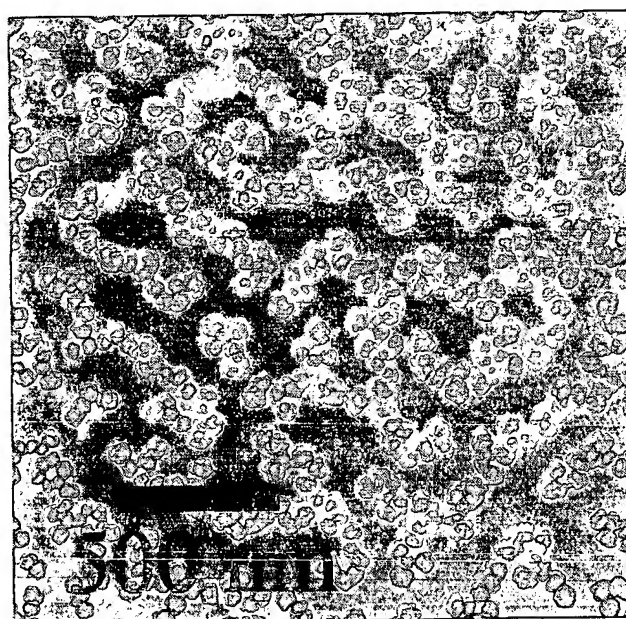


FIGURE 3 Nanoparticles formed under 100 Torr He, after 450 pulses at 0.6 J/cm^2

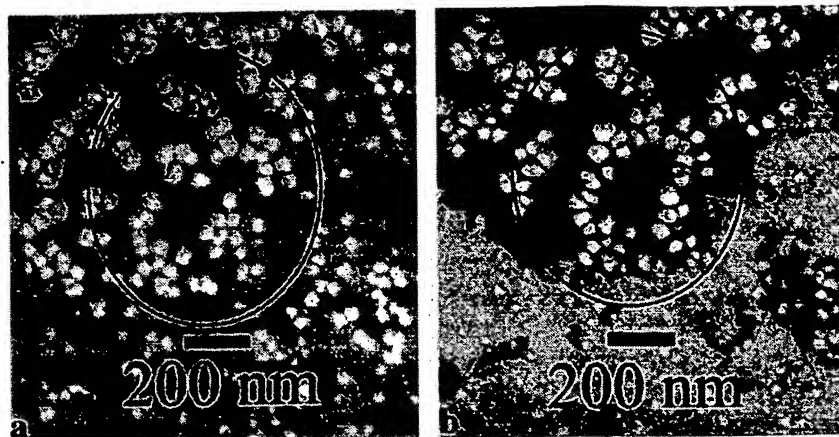


FIGURE 4 Motion of nanoparticles followed inside *encircled region*. a 500 pulses; b 700 pulses. Fluence: 0.6 J/cm^2 ; He pressure: 100 Torr

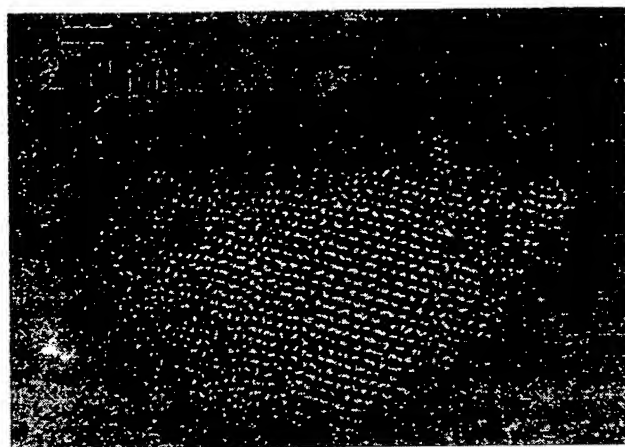


FIGURE 5 SEM image showing film clustering, and nanoparticle formation and ordering. Specimen irradiated with 200 pulses at 1 J/cm^2 under 100 Torr He

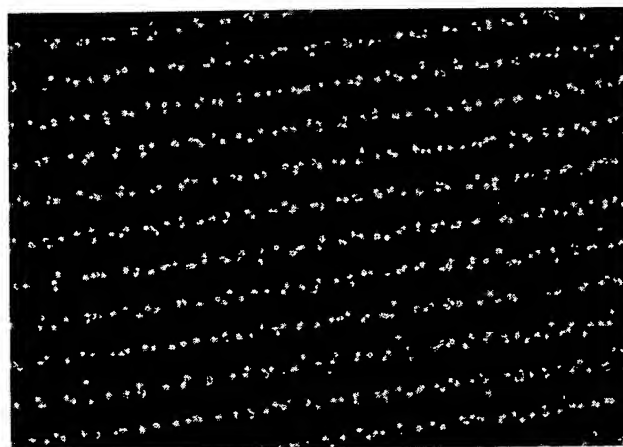


FIGURE 6 Laser-induced nanoparticle linear array in the vicinity of a microstructured region of the surface. Fluence: 1 J/cm^2 ; 0.5 Torr He; 200 pulses

strate surface adjacent to the microstructured zone. Figure 5 illustrates the evolution of the film, demonstrating that the nanoparticles grew in the substrate, consuming the film, and became aligned as they were being irradiated.

The nanoparticle ordered array shown in Fig. 6, has a line-spacing close to 248 nm and extends over microscopic regions with few perturbations in the alignment. This array developed in the immediate vicinity of the cone microstructure region. Characterization of the nanocrystals by using Auger electron spectroscopy demonstrated that the nanoparticle consisted of silicon cores covered with a very thin sheath of oxide.

Certain aspects of the nanoparticle alignment phenomenon suggest that it could be associated with the LIPSS phenomenon. Similar to the conditions reported for LIPSS development, the alignment was initially observed just above the melting threshold, and occurred in a narrow laser fluence range above this threshold. In almost every case, although not in all of them, for normal incidence, the particles aligned along the rectangular beam short axis, which corresponded to the direction where the E field was at a maximum. In a second set of experiments, in which a fine wire ($100 \mu\text{m}$) crossing the beam was imaged on a flat Si substrate surface, a linear alignment of nanoclusters occurred within the interference fringe pattern resulting from the diffraction of light by the wire. An AFM image taken from the same specimen shown in Fig. 6 re-

veals that nanoparticles were located on the valleys of LIPSS (Fig. 7). Lack of contrast prevented observation of the smooth undulations of LIPSS by SEM.

At variance with the LIPSS experiments described in the preceding section, the alignment of nanoparticles did not require polarized light; the presence of an extended defective region was sufficient. Next, we used p-polarized light, and aligned nanoparticles were produced on a flat surface, without the need for an initial microcone structure. Nanoparticle arrays aligned normal to the direction of the electric field. An experiment that illustrates well the process of nanoparticle production and alignment with size selection was done by irradiating the silicon surface with polarized light at an average energy density higher than 1 J/cm^2 . The irradiated area was rectangular and we utilized a beam size of approximately $7 \text{ mm} \times 3 \text{ mm}$. All over the edges, where the beam energy tapered off and within a width of $\sim 0.4 \text{ mm}$, an aligned array of $\sim 30\text{-nm}$ -diameter nanoparticles was generated. A microstructure consisting of long surface waves was produced in the central portion of the irradiated region where the energy was too high for particle formation. The production of this microstructure indicates that very significant ablation could have taken place in the central region of the spot. AFM scans reveal an abrupt change in the spatial and size distribution of nanoparticles at the sides of the edges of the laser shot, into

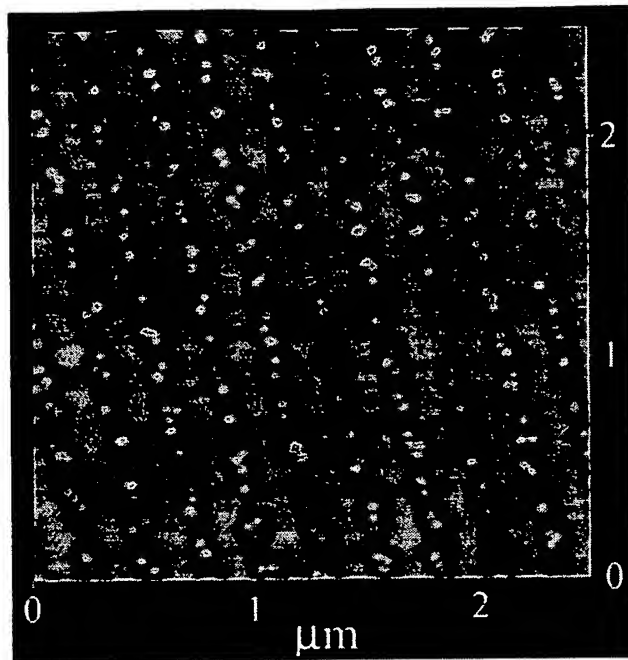


FIGURE 7 AFM image of the same surface as in Fig. 6

the unirradiated region. Instead of the highly organized array of small, fairly uniformly sized nanoparticles detected inside the irradiated edge, a completely random distribution of much larger nanoparticles with a wide size distribution was found to cover the adjacent unirradiated area.

Using p-polarized light, the angle of incidence of the laser beam was changed and it was found that the nanoparticle line spacing followed (1) with the minus sign in the denominator, i.e., the line-spacing increased as the angle of incidence was increased. This result strongly suggests that similar mechanisms are responsible for the formation of nanochannels and for nanoparticle alignment.

The results just described, whereby spontaneous alignment of silicon nanoparticles form regular arrays as a result of pulsed-laser irradiation of a silicon substrate, opens the possibility of using UV lasers as manipulators of nanoparticles on a large scale, on the order of millimeters.

5 Silicon nanostructuring atop a laser-produced microcone template

The formation of microcones has been explained by a mechanism similar to that used to explain the formation of whiskers in silicon [6–8]. The cone microstructure appears first to present a natural limit – as far as a minimum dimension is concerned – for laser-induced structuring of a surface with self-organized tips. This limitation arises from the formation and growth mechanisms of the cone and the fact that it starts at a surface that is melted throughout. Once a cone is formed, and its subsequent growth is accomplished by preferential re-deposition of material at its laser-melted tip, continuing irradiation under the same conditions will produce a rise in the cone first and result in its fall at later stages. However, we have found that a change in processing conditions could ben-

efit from a well developed microcone structure, using it as a template for a finer structure.

A silicon target, microstructured as shown in Fig. 1c, was irradiated at 0.5 J/cm^2 in a He atmosphere at 10 Torr. It was first noticed that 2000 pulses produced the emergence at the microcone tips of small protrusions $\sim 100 \text{ nm}$ in diameter and a few nanometers in height (Fig. 8). The sequence of images presented in Fig. 9 shows the growth of one nanocolumn as a function of the number of laser pulses. Figure 9a shows the cone tip of the initial microstructured surface for which the nanocolumn evolution has been followed. We always observed a small tip at the top of the microcones, and as we continued the irradiation at low energy, the protrusion grew and a flat depression was formed around it (Fig. 9b and c). A careful examination of the images shows that the low-energy irradiation only produced melting at the very top of the cone tip. The fluence used in these experiments (referred to a flat surface) was very close to the melting threshold and it decreased from the center of the cone tip towards the sides due to the tip curvature. Thus, these irradiation conditions explain the highly localized melting. As the irradiation was continued, the depression around the protrusion disappeared (Figs. 9d–f), and the protrusion developed into a nanocolumn, while a multitude of very small protrusions appeared at its base (Fig. 9e). Finally, after 10 000 pulses the nanocolumn had a height of $3.1 \mu\text{m}$ and a diameter of 200 nm , giving an aspect ratio of 15. Due to the nanosecond pulse duration, silicon transport to the top could only have taken place in the liquid or gas phase. The liquid could only be removed from the immediate vicinity where melting took place. The small and flat depression around the nanocolumn cannot account for the extra mass of silicon from the nanocolumn and the protrusions that mushroomed around it.

The chemical composition of the nanocolumns grown in He was measured using the electron beam of a SEM at normal incidence, focused at the center of the nanocolumn in a spot of 150-nm -diameter. Only the chemical composition of the nanocolumn was measured, because the probe region extends to $\sim 1.5 \mu\text{m}$ in depth, which is significantly less than the column height. It was found that the nanocolumns were made of silicon with less than 2 at. % of oxygen, while the amount of oxygen measured in the substrate was less than 1%. The error

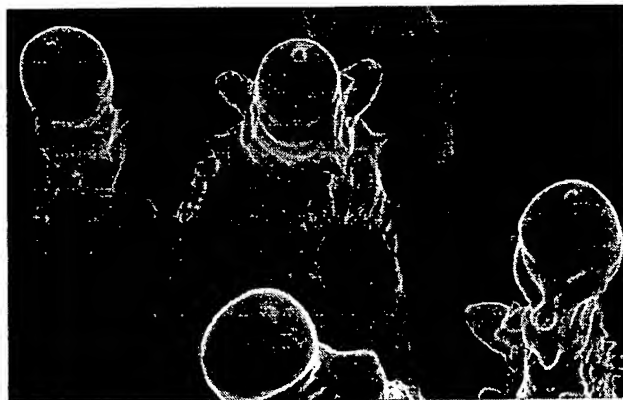


FIGURE 8 Nanocolumns growing on microcone tips. Fluence: 0.5 J/cm^2 , 2000 pulses, He pressure: 10 Torr

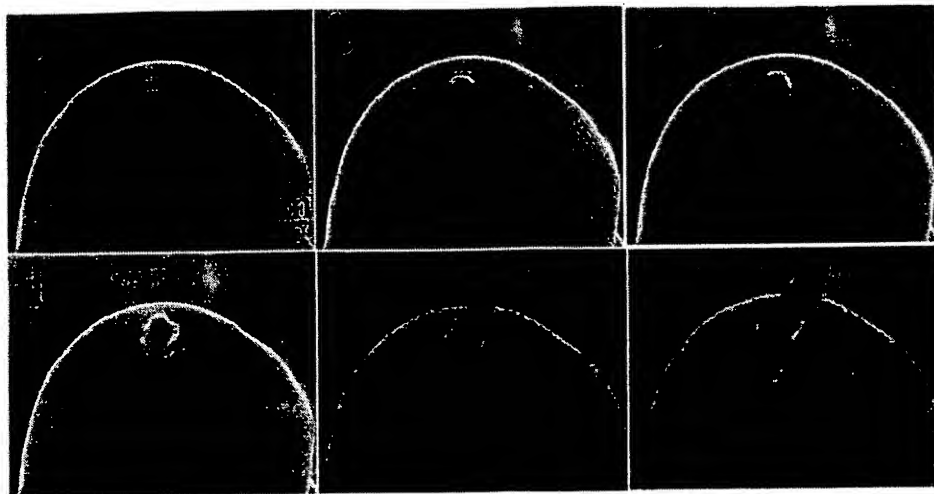


FIGURE 9 Nanocolumn evolution upon laser irradiation at 0.5 J/cm^2 in 10 Torr He. a initial cone tip; b 1000 pulses; c 2500 pulses; d 5000 pulses; e 8000 pulses; f 10000 pulses



FIGURE 10 Tip of same nanocolumn as shown in Fig. 8, after 15 000 pulses

in the electron dispersion X-ray spectroscopy measurements was on the order of 1%.

The laser fluence at the bottom of the microcones is enhanced by multiple reflections promoting ablation, and due to the background pressure, ablated material is partly backscattered and can be trapped at the melted nanocolumn tip. It has been calculated that the intensity at the bottom of the microcones, tens of micrometers below the surface, is increased over 4-fold [8]. The process of deposition is clearly visible after 15 000 pulses because a film covers a large portion of the substrate. Also, after 15 000 pulses the top of the nanocolumns become significantly enlarged and the deposition process is further revealed by the multiple small protrusions that cover the tip (Fig. 10). The low ablation rate is reflected in the extremely low growth rate of nanocolumns, 0.2 nm per pulse.

Irradiation in vacuum, for which the trapping of ablated material is more difficult because there is no buffer gas atmosphere, shows that after 2500 pulses small protrusions

similar to those shown in Fig. 9c are formed at the top of the microcones. However, in vacuum these protrusions do not grow additionally and after 10 000 pulses they tend to flatten.

These experimental observations suggest that the initial protrusion at the top of the microcones (Fig. 9b and c) is most likely a result of the solidification process of the laser-melted pool. When the nano-protrusions reach a certain size, deposition of silicon strongly increases their length by continuing irradiation under helium, keeping the diameter approximately constant (Fig. 9e and f). This last process appears to be similar to that described for microcolumn growth [4].

ACKNOWLEDGEMENTS This research was sponsored by the National Science Foundation Grant No. DMR-9901238.

REFERENCES

- 1 F. Sanchez, J.L. Morenza, R. Aguiar, J.C. Delgado, M. Varela: *Appl. Phys. Lett.* **69**, 620 (1996); F. Sanchez, J.L. Morenza, R. Aguiar, J.C. Delgado, M. Varela: *Appl. Phys. A* **66**, 83 (1998); F. Sanchez, J.L. Morenza, V. Triik: *Appl. Phys. Lett.* **75**, 3302 (1999)
- 2 T.-H. Her, R.J. Finlay, C. Wu, S. Deliwala, E. Mazur: *Appl. Phys. Lett.* **73**, 1673 (1998); T.-H. Her, R.J. Finlay, C. Wu, E. Mazur: *Appl. Phys. A* **70**, 383 (2000)
- 3 V.V. Voronov, S.I. Dolgaev, S.V. Lavrishchev, A.A. Lyalin, A.V. Simakin, G.A. Shafeev: *Phys. Vib.* **7**, 131 (1999); S.I. Dolgaev, S.V. Lavrishchev, A.A. Lyalin, A.V. Simakin V.V. Voronov, G.A. Shafeev: *Appl. Phys. A* **73**, 177 (2001)
- 4 A.J. Pedraza, J. Fowlkes, D.H. Lowndes: *Appl. Phys. Lett.* **74**, 2322 (1999)
- 5 J. Pedraza, J.D. Fowlkes, D.H. Lowndes: *Appl. Phys. Lett.* **77**, 3018 (2000)
- 6 J.D. Fowlkes, A.J. Pedraza, D.H. Lowndes: *Appl. Phys. Lett.* **77**, 1629 (2000)
- 7 J. Pedraza, S. Jesse, Y. Guan, J.D. Fowlkes: *J. Mater. Res.* **16**, 3599 (2001)
- 8 S. Jesse, A.J. Pedraza, J.D. Fowlkes, J.D. Budai: *J. Mater. Res.* **17**, 1002 (2002)
- 9 P.A. Temple, M.J. Soileau: *IEEE J. Quantum Electron.* **QE-17**, 2067 (1981)
- 10 P.M. Fauchet, E. Siegman: *Appl. Phys. Lett.* **40**, 824 (1982)
- 11 Z. Guosheng, P.M. Fauchet, E. Siegman: *Phys. Rev. B* **26**, 5366 (1982)
- 12 J.F. Young, J.S. Preston, H.M. van Driel, J.E. Sipe: *Phys. Rev. B* **27**, 1155 (1982)
- 13 S.R.J. Brueck, D.J. Ehrlich: *Phys. Rev. Lett.* **48**, 1678 (1982)
- 14 S.A. Akhmanov, V.I. Emel'yanov, N.I. Koroteev, V.N. Seminogov: *Sov. Phys. Usp.* **28**, 1084 (1986)

- 15 D. Bäuerle: *Laser Processing and Chemistry*, 3rd edn. (Springer-Verlag, Berlin 2000) p. 571
- 16 F. Keilmann, Y.H. Bai: *Appl. Phys. A* **29**, 9 (1982)
- 17 J.F. Figueira, S.J. Thomas: *Appl. Phys. B* **28**, 267 (1982)
- 18 F. Keilmann: *Phys. Rev. Lett.* **51**, 2097 (1983)
- 19 J.F. Young, J.E. Sipe, H.M. van Driel: *Phys. Rev. B* **30**, 2001 (1984)
- 20 M. Bolle, S. Lazare: *J. Appl. Phys.* **73**, 3516 (1993)
- 21 P.E. Dyer, R.J. Farley, R. Giedl, D.M. Karnakis: *Appl. Surf. Sci.* **96–98**, 537 (1996)
- 22 M. Csete, Z. Bor: *Appl. Surf. Sci.* **133**, 5 (1998)
- 23 J.E. Sipe, J.F. Young, J.S. Preston, H.M. van Driel: *Phys. Rev. B* **27**, 1141 (1982)
- 24 J.D. Fowlkes, A.J. Pedraza, D.A. Blom, H.M. Meyer III: *Appl. Phys. Lett.* **80**, 3799 (2002); *Virtual J. Nanoscale Sci. Technol.* May 27, (2002)

Vacuum tunneling of superconducting quasiparticles from atomically sharp scanning tunneling microscope tips

S. H. Pan, E. W. Hudson, and J. C. Davis^{a)}

Department of Physics, University of California, Berkeley, Berkeley, California 94720

(Received 30 July 1998; accepted for publication 21 September 1998)

We report on the study of atomically sharp superconducting tips for scanning tunneling microscopy and spectroscopy. The results clearly show vacuum tunneling of superconducting quasiparticles from atomically sharp tips. Observed deviations of the energy gap of the superconducting tip from its bulk value are attributed to the proximity effect. We show that a combination of a superconducting tip and an atomic resolution scanning tunneling microscope provides a means of achieving very high resolution local spectroscopy. We also discuss how this combination paves the way for a number of important applications. © 1998 American Institute of Physics.

[S0003-6951(98)04446-5]

Since early in its history, scanning tunneling microscopy (STM) with nonsuperconducting tips has been used to successfully study the local properties of superconducting samples.¹⁻⁴ Interestingly, although it has long been proposed,⁵ use of superconducting tips for STM has not been achieved. We note that a number of important experiments have used scanning tunneling microscopes to create adjustable microscopic junctions with superconducting electrodes.⁶⁻⁸ We distinguish these techniques from the use of a sharp superconducting tip (having one or a few atoms at the end), with vacuum tunneling, for atomically resolved microscopy and spectroscopy. One might naturally ask whether such a sharp tip could even exhibit a superconducting density of states (DOS) at the end. Recently, Yazdani *et al.* noted the existence of a BCS single electron excitation spectrum above a normal metal adatom on a superconducting Nb substrate.⁹ This implies that atomically sharp superconducting STM tips might be achievable. In this letter we report the successful realization of such tips, and describe their application to the study of both normal and superconducting samples.

For this work, we use a very-low-temperature STM,¹⁰ which has spectroscopic resolution better than 30 μ V at its base temperature of 250 mK. The superconducting tips are made from 0.2 mm diam Nb wire by mechanical sharpening. The tip installation is carried out with the STM open to air at room temperature. The STM chamber is then sealed, evacuated to 10^{-6} Torr, and cooled to 4.2 K. The natural oxide of Nb at the apex of the tip is removed, and the tip is further sharpened, by field emission against a Au target in cryogenic ultrahigh vacuum at 4.2 K. After this process, the sharpness of the tip is verified by identification of atomic scale features on the Au surface.

Next, the relationship between tunneling current I and tip displacement from the surface z is recorded to confirm the characteristic exponential behavior of vacuum tunneling [$I \propto \exp(-z/z_0)$ where z_0 is a decay constant]. From these data, the effective barrier height, which represents the convoluted work function of the tip and the sample, can be

extracted.¹¹ As an example, the results of a I vs z measurement for a Nb tip is plotted in log/linear format in Fig. 1(a). The curve is linear over three decades of current, which confirms the vacuum nature of the tunneling, and a work function of 2.9 eV is deduced from its slope.

To evaluate the superconducting properties of this Nb tip, the differential conductance $G(V) = dI/dV$ of tunneling between tip and sample is measured as a function of bias voltage V .¹² This function is a measure of the convoluted local DOS of the sample and the tip.¹³ We use the Au field

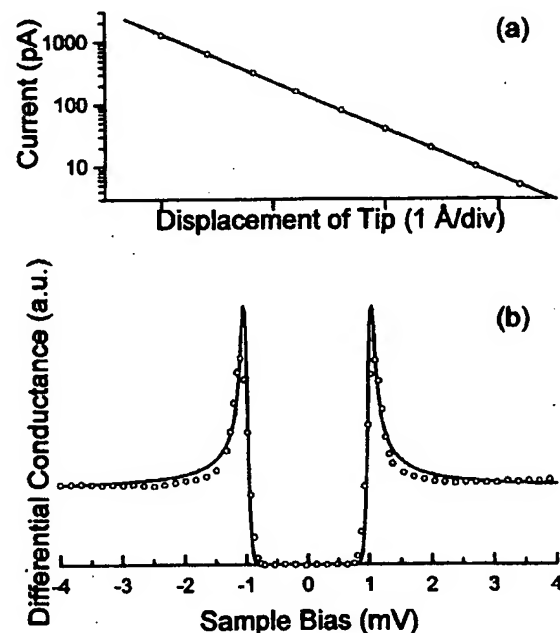


FIG. 1. (a) A log/linear plot of the tunneling current vs displacement of a Nb tip from a Au surface. The circles are the measured data, and the solid line is the linear fit. The exponential relationship over three decades of current indicates the vacuum nature of the tunneling. (b) Tunneling conductance vs sample bias for the same Nb tip at 335 mK. The solid line is the calculated conductance using a BCS DOS and an energy gap $\Delta_{\text{tip}}(0) = 1.0$ meV. The circles are the measured data (only a fraction of the measured data points are shown to allow clear display of the underlying calculated curve). The spectrum indicates a superconducting quasiparticle DOS at the tip end.

^{a)}Electronic mail: jodavis@socrates.berkeley.edu

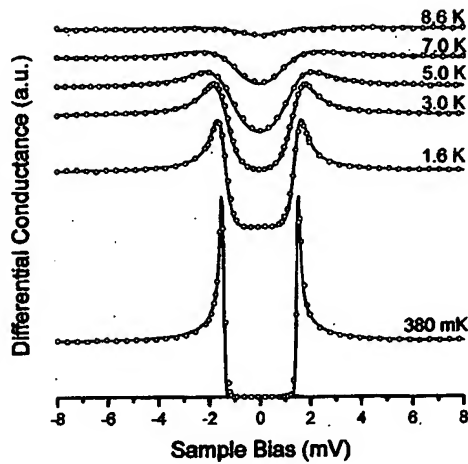


FIG. 2. Measured differential conductance spectra (circles) for tunneling between a Nb tip and a Au surface at several temperatures. The spectra are displaced vertically from each other for clarity. The solid lines are the calculated conductance using a BCS DOS with $\Delta_{\text{tip}}(0) = 1.47$ meV and the temperatures shown. The excellent agreement of the data and the calculations confirms that the temperature dependence of the tip DOS is very similar to that of bulk Nb.

emission target as the sample. Figure 1(b) shows the resulting differential conductance spectrum taken at 335 mK. It clearly demonstrates a superconducting quasiparticle DOS, as evidenced by the zero of conductance below the gap voltage and the high peaks at the gap edge. To clarify that the superconducting features in this spectrum are due to the tip, and not due to possible deposition of Nb onto the surface during field emission, this measurement is performed at several different locations separated by more than 100 nm from the location where the field emission was performed. The absence of significant variations between the spectra at different locations indicates that the energy gap in the DOS observed is that of the tip.

It is interesting to note that the measured superconducting energy gap value of the tip Δ_{tip} varies from tip to tip after

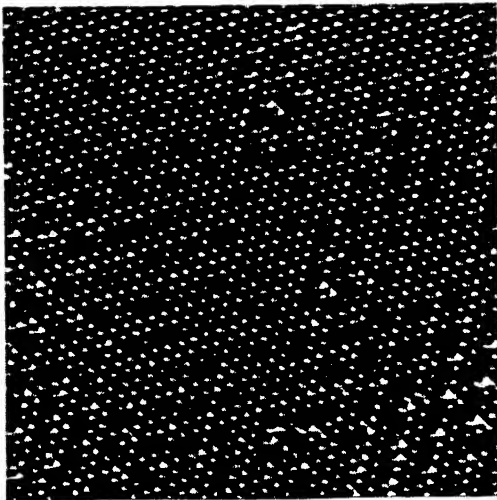


FIG. 3. Topographic image (150 Å square) of a NbSe₂ surface acquired at 4.2 K in constant current mode with the superconducting tip whose tunneling spectrum is shown in Fig. 2. A charge density wave pattern is clearly visible. The atomic resolution of the image indicates that this superconducting tip is atomically sharp.

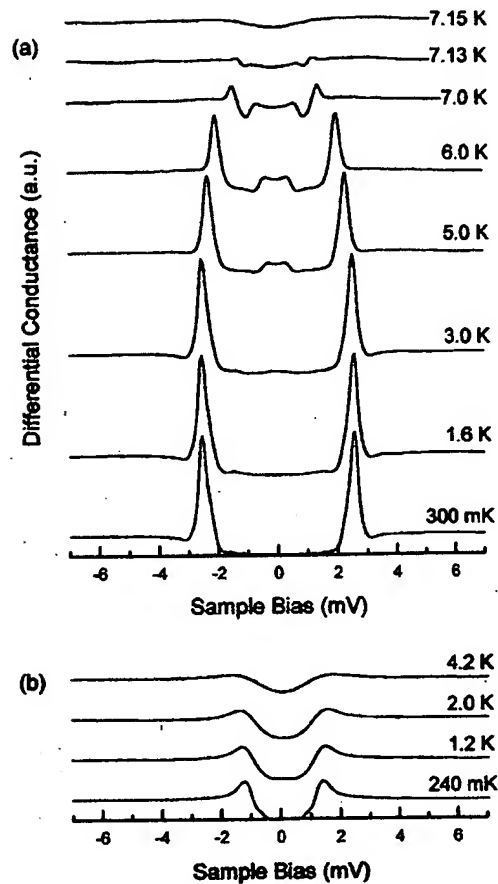


FIG. 4. (a) Measured differential conductance spectra for tunneling between a superconducting Nb tip and a NbSe₂ surface. The characteristic SS tunneling peaks $\Delta_{\text{tip}} + \Delta_{\text{NbSe}_2}$ and $\Delta_{\text{tip}} - \Delta_{\text{NbSe}_2}$ vary in voltage and change in magnitude, with temperature, as expected. (b) Measured differential conductance spectra for tunneling (NS) between a PtIr tip and a NbSe₂ surface. Comparison between the SS and NS tunneling spectra, plotted in the same scale, shows the dramatic enhancement in sharpness of the features obtained with a superconducting tip.

the field emission process, ranging from a few tenths of an meV to near the bulk gap value of Nb [1.53 meV at $T = 0$ K (Ref. 14)]. The origin of this deviation is not fully understood. One possible explanation is that the superconductivity observed at the end of the tip has propagated from the bulk due to the proximity effect.¹⁵ Thus the measured gap will depend on the dimensions, structure, and composition of the apex of the tip, which can be modified during field emission.

In Fig. 2, differential conductance spectra from another Nb tip (prepared and evaluated for its work function and sharpness as described above) are shown from 8.6 K to 380 mK. Each trace is displaced vertically for clarity. One can clearly see the superconducting gap in the DOS developing at the tip with falling temperature. The solid lines in Fig. 2 are the expected spectra for each temperature, calculated from a BCS DOS using a value of the energy gap for the tip $\Delta_{\text{tip}}(0) = 1.47$ meV. Note that the agreement between the measured data and calculations is much better than in Fig. 1(b). In general, the smaller the deviation of the measured gap from its bulk value, the better the agreement with the BCS DOS, especially near the edge of the gap. This is an expected consequence of the proximity effect.¹⁶

To study superconducting-tip scanning tunneling mi-

croscopy on a superconductor, we now use this tip to perform measurements on a sample of NbSe₂. This is a well-studied layered material, which shows a charge density wave, and has a superconducting phase transition at $T_c = 7.2$ K. The superconducting energy gap, as measured by STM, is $\Delta_{\text{NbSe}_2}(0) = 1.11$ meV.³ A NbSe₂ single crystal sample is cleaved *in situ* at 4.2 K and exchanged for the Au sample. Figure 3 shows an image of the NbSe₂ surface at $T = 4.2$ K, taken with the tip whose tunneling conductance spectra are shown in Fig. 2. Both the atomic lattice on the surface and the charge density wave are clearly resolved. This confirms that the tip is atomically sharp. Again, conductance spectroscopy is carried out on this NbSe₂ surface as a function of temperature and the results are displayed in Fig. 4(a).

The two pairs of peaks in Fig. 4(a) are characteristic of the superconducting–superconducting (SS) nature of the tunneling, and clearly distinguish it from normal–superconducting (NS) tunneling. The experimental values of $V = \pm (\Delta_{\text{tip}} \pm \Delta_{\text{NbSe}_2})/e$ at which they occur are in excellent agreement with the values calculated from the BCS theory¹⁷ at all temperatures measured. This confirms not only the existence of a superconducting DOS at the end of the tip, but also that tunneling in SS-STM is physically similar to that in planar junctions, albeit in a junction of far smaller area.

The use of superconducting tips in low-temperature scanning tunneling microscopes has a number of significant advantages. Most important of these is the improvement in spectroscopic resolution when compared to normal–tip STM. This is due to the sudden rise in conductance at the gap edge and the associated high peak in the DOS of the superconducting tip.¹⁸ An example of this can be seen by comparing the SS tunneling of Fig. 4(a) with the NS tunneling of Fig. 4(b), where we show the conductance spectra acquired on NbSe₂ with a nonsuperconducting PtIr tip. There is a dramatic enhancement of sharpness of the features in the spectrum obtained with a superconducting tip, which could prove significant in many scanning tunneling spectroscopy (STS) measurements, since it exists even at the commonly available temperature of 4.2 K.

Of even greater significance is the fact that superconducting-tip STM opens the door for many important future applications. One example is spin polarized STM and STS. Here, the Zeeman splitting of the quasiparticle DOS for the two spin orientations in the superconducting tip can provide a spin polarized electron source⁵ capable of being scanned, with atomic resolution, over the surface to be studied. Another example is Josephson tunneling in SS-STM. This would be significant in its own right, since it would provide a new type of tunable Josephson junction. It could also become a useful instrument to study, for example, spatial variations of the order parameter in exotic superconductors.¹⁹

In conclusion, reliable operation of atomically sharp su-

perconducting Nb tips, with vacuum tunneling, in low-temperature STM and STS has been achieved. The measured energy gap at the ends of these tips varies, and we attribute deviations from the bulk value to the proximity effect. SS tunneling between a Nb tip and a NbSe₂ surface is studied from 250 mK to 9 K, and compared to NS tunneling with a PtIr tip under similar conditions. This mode of STM not only provides a much improved spectroscopic resolution, but also opens the door for many future applications, including scanning spin-polarized electron tunneling, and scanning Josephson tunneling.

The authors thank A. L. de Lozanne, J. Moreland, J. F. Zasadzinski, and R. E. Packard for valuable conversations. The authors thank A. Zettl for his generosity in providing the NbSe₂ crystals. This work was supported by the NSF under Grant No. DMR 94-58015 and by the David and Louise Packard Foundation.

¹A. L. de Lozanne, S. A. Elrod, and C. F. Quate, *Phys. Rev. Lett.* **54**, 2433 (1985).

²J. R. Kirtley, S. I. Raider, R. M. Feenstra, and A. P. Fein, *Appl. Phys. Lett.* **50**, 1607 (1987).

³H. F. Hess, R. B. Robinson, R. C. Dynes, J. M. Valles, Jr., and J. V. Waszczak, *Phys. Rev. Lett.* **62**, 214 (1989).

⁴J. R. Kirtley, *Int. J. Mod. Phys. B* **4**, 201 (1990).

⁵R. Meservey, *Phys. Scr.* **38**, 272 (1988).

⁶Q. Chen, K.-W. Ng, A. E. Manzi, and H. L. Luo, *Phys. Rev. B* **49**, 6193 (1994).

⁷Y. DeWilde, N. Miyakawa, P. Guptasarma, M. Iavarone, L. Ozyuzer, J. F. Zasadzinski, P. Romano, D. G. Hinks, C. Kendziora, G. W. Crabtree, and K. E. Gray, *Phys. Rev. Lett.* **80**, 153 (1998).

⁸H. Murakami, S. Ohbuchi, and R. Aoki, *Physica C* **235-240**, 1887 (1994).

⁹A. Yazdani, B. A. Jones, C. P. Lutz, M. F. Crommie, and D. M. Eigler, *Science* **275**, 1767 (1997).

¹⁰S. H. Pan, E. W. Hudson, and J. C. Davis, *Rev. Sci. Instr.* (to be published).

¹¹J. H. Coombs and J. B. Pethica, *IBM J. Res. Dev.* **30**, 455 (1986); N. Garcia, *ibid.* **30**, 533 (1986).

¹²All differential conductance spectra measurements in this experiment were performed using a lock-in technique with a modulation amplitude of 50 μ V. The junction resistance was set to 100 M Ω at a bias voltage of 8 mV (well outside the superconducting energy gap).

¹³R. J. Hamers, *Annu. Rev. Phys. Chem.* **40**, 531 (1989).

¹⁴P. Townsend and J. Sutton, *Phys. Rev.* **128**, 591 (1962).

¹⁵S. Guéron, H. Pothier, N. O. Birge, D. Esteve, and M. H. Devoret, *Phys. Rev. Lett.* **77**, 3025 (1996).

¹⁶J. F. Zasadzinski (private communication). One of the signatures of the proximity effect is the appearance of two dips directly outside of the peaks at each side of the gap edge. In SS tunneling this can be seen more clearly because there will be no thermal smearing due to a normal state electrode [as evidenced in Fig. 4(a)]. One can also approximately simulate SS tunneling effects by convoluting a SN tunneling curve with itself. Self-convolutions of both the data in Figs. 1(b) and 2(a) show such dips, whereas the self-convolution of the data in Fig. 4(b) does not. This indicates that the proximity effect is indeed only in the tip.

¹⁷E. L. Wolf, *Principles of Electron Tunneling Spectroscopy*, International series of monographs on physics, Vol. 71 (Oxford University Press, New York, 1985), p. 105.

¹⁸L. Solymar, *Superconductive Tunneling and Applications* (Wiley-Interscience, New York, 1972), pp. 112 and 113.

¹⁹M. Franz, C. Kallin, P. I. Soininen, A. J. Berlinsky, and A. L. Fetter, *Phys. Rev. B* **53**, 5795 (1996).

**This Page is Inserted by IFW Indexing and Scanning
Operations and is not part of the Official Record**

BEST AVAILABLE IMAGES

Defective images within this document are accurate representations of the original documents submitted by the applicant.

Defects in the images include but are not limited to the items checked:

- ☐ BLACK BORDERS
- ☐ IMAGE CUT OFF AT TOP, BOTTOM OR SIDES
- ☐ FADED TEXT OR DRAWING
- ☐ BLURRED OR ILLEGIBLE TEXT OR DRAWING
- ☐ SKEWED/SLANTED IMAGES
- ☐ COLOR OR BLACK AND WHITE PHOTOGRAPHS
- ☐ GRAY SCALE DOCUMENTS
- ☐ LINES OR MARKS ON ORIGINAL DOCUMENT
- ☐ REFERENCE(S) OR EXHIBIT(S) SUBMITTED ARE POOR QUALITY
- ☐ OTHER: _____

IMAGES ARE BEST AVAILABLE COPY.

As rescanning these documents will not correct the image problems checked, please do not report these problems to the IFW Image Problem Mailbox.